Southern Ocean Cloud Properties Derived from CAPRICORN and MARCUS Data

Gerald G. Mace[1], Alain Protat[2,5], Ruhi S. Humphries[3,5], Simon P. Alexander[4,5], Ian M. McRobert[6], Jason Ward[7], Paul Selleck[3], Melita Keywood[3]

1. Department of Atmospheric Sciences, University of Utah
2. Australian Bureau of Meteorology, Melbourne, Australia
3. Climate Science Centre, CSIRO Oceans and Atmosphere, Aspendale, Australia
4. Australian Antarctic Division, Kingston, Tasmania, Australia
5. Australian Antarctic Programme Partnership, Institute for Marine and Antarctic Studies, University of Tasmania, Hobart, Australia
6. Engineering and Technology Program, CSIRO Oceans and Atmosphere, Hobart, Australia
7. Climate Science Center/Atmospheric Composition and Chemistry/Aerosols, Oceans and Atmosphere, CSIRO

Submitted to Journal of Geophysical Research, June, 2020

Corresponding Author Information:
Gerald “Jay”Mace, Professor
Department of Atmospheric Sciences, University of Utah
135 South 1460 East Rm 819 (819 WBB)
Salt Lake City, Utah, 84112-0110
Cell Phone: 801 201 7944
Office Phone: 801 585 9489
Email: jay.mace@utah.edu
Fax: 801 860 0381

Abstract: The properties of Southern Ocean (SO) liquid phase non precipitating clouds (hereafter clouds) are examined using shipborne data collected during the Measurements of Aerosols, Radiation and Clouds over the Southern Ocean (MARCUS) and the Clouds Aerosols Precipitation Radiation and atmospheric Composition Over the SoutheRN ocean (CAPRICORN) I and II campaigns that took place in the Southern Ocean south of Australia during 2016 and late 2017 into early 2018. The cloud properties are derived using W-band radar, lidar, and microwave radiances using an optimal estimation algorithm. The SO clouds tended to have larger liquid water paths (LWP, 115 ±117 g m-2), smaller effective radii (r_e, 8.7 ±3um), and higher number concentrations (N_d, 90 ±107 cm^{-3}), than typical values of eastern ocean basin stratocumulus. The clouds demonstrated a tendency for the LWP to increase with N_d presumably due to precipitation suppression up to N_d of approximately 100 cm^{-3} when mean LWP decreased with increasing N_d. Due to higher optical depth, cloud albedos were less susceptible to changes in N_d compared to subtropical stratocumulus. The high latitude clouds observed along and near the Antarctic coast presented a distinctly bimodal character. One mode had the properties of marine clouds further north. The other mode occurred in an aerosol environment characterized by high cloud condensation nuclei concentrations and elevated sulfate aerosol without any obvious continental aerosol markers that had much higher N_d, smaller r_e and overall higher LWP suggesting distinct sensitivity of the clouds to seasonal biogenic aerosol production in the high latitude regions.

1. Introduction

The clouds fields of the Southern Ocean have emerged as one of the lynchpins in our understanding of the Earth's climate system (Tan et al., 2016; Frey and Kay, 2017, Kay et al., 2016; Gettelman et al., 2020). While the circumpolar storm tracks are well known for strong frontal systems wrapping deep midlatitude cyclones, it is the accompanying fields of low level clouds, based mostly in the marine boundary layer (MBL), that seem to be critical to understanding the radiative energy balance of this region (Bodas-Salcedo et al., 2012, 2014, 2016; 2019). These low-level clouds evolve from cumuliform to stratiform from just behind the cold fronts to the upstream ridge. Inspired by the findings of Trenberth and Fasullo (2010) who showed that too much solar energy is absorbed at the surface, studies have increasingly focused on the ubiquity of supercooled liquid water in SO supercooled clouds where predictions too aggressively reduce cloud cover through ice phase precipitation processes (Vergara-Temprado et al., 2018; Frey and Kay, 2017). Recent modelling studies have mitigated this bias through various means and have thereby shown the sensitivity of the climate system to these SO MBL clouds (Tan et al., 2016; Kay et al., 2016). Recent work (Mace et al., 2020; Mace and Protat, 2018a; O'Shea et al., 2017), however, is suggesting that more mixed phase clouds are found in the Southern Ocean than diagnosed from earlier spaceborne lidar data (Hu et al., 2009) even though the concentrations of Ice Nucleating Particles are found to be extremely low (McCluskey, et al., 2018).

How the properties of liquid phase clouds – especially supercooled liquid phase clouds – vary across the SO remains an important topic. While the meteorology of the SO is predictable, variations in factors that control the local and regional aerosol properties vary considerably from regions north of the Antarctic Circumpolar Current (ACC) to the marginal seas along the Antarctic (Armour et al., 2016; Fossum et al., 2018). While seasonally varying sea surface temperatures and sea ice contribute to the cloud variability (Huang et al., 2016), the Antarctic Circumpolar Current essentially divides the SO into lower latitude temperate and high latitude marginal seas. Especially in the high latitude SO, seasonal biological productivity results in significant seasonal oscillations in sulfate aerosol sources (Shaw, 1988; O'Dowd et al., 1997; Humphries et al., 2016; Ayers and Gras, 1991) that appear to drive variability in cloud properties across the entire oceanic basin between winter and summer (McCoy et al., 2015; Mace and Avey, 2017). Liquid clouds existing within this highly variable environment respond both to the large-scale meteorological forcing and moisture transports (McCoy et al. 2019; Klein et al., 2017; Kelleher and Grise, 2019) and to the local aerosol environment. The large-scale environment provides the thermodynamic conditions for producing clouds while the latter controls the detailed processes that determine when and how low-level clouds precipitate (Savic-Jovcic and Stevens, 2008) and influence the local surface energy budget (Protat et al., 2017).

In this study, we examine a particular genre of MBL clouds that form a significant component of the total cloud population of the SO. Table 1 illustrates that geometrically thin and non-precipitating MBL clouds feature prominently within the larger context of the SO cloud climatology. We find that the SO, defined here as the circumpolar latitude belt from 45 S to 70 S, has an overall cloud fraction of 86%. Of this overall cloud cover, 63% are

single layer. The MBL-based clouds can be roughly divided into two classes. Clouds with geometric thicknesses in excess of 1 km tend to be mostly precipitating (as defined by CloudSat) while roughly half of the MBL clouds have geometric thicknesses less than 1 km and exist as non-precipitating liquid phase layers. Because the non-precipitating thin clouds have radar reflectivities inconsistent with precipitation, or often exist within 1 km of the surface, they are largely unobserved by CloudSat (Marchand et al., 2008; Alexander and Protat, 2018) and, therefore, their properties are not well known.

Our objective in this study is to examine the microphysical properties of the non-precipitating clouds and quantify how they vary latitudinally within the Southern Ocean sector bounded by the East Antarctic coastline to Hobart (43S) and from 60E to 160 E using ship-based remote sensors from voyages by Australian Research Vessels between 2016 and 2018. In particular, we examine dependencies between cloud droplet number (Nd), effective radius (re), and liquid water path (LWP) with various factors over the space and time covered by the observations. We consider how these clouds influence the surface solar radiation and the Top Of Atmosphere (TOA) albedo. We also consider how the cloud properties are associated with well-defined aerosol regimes characterized during the campaigns.

Table 1: Vertical occurrence data from CloudSat (Stephens et al., 2008) and CALIPSO (Winker et al., 2009) between 2007-2010 using the combined characterization of Mace and Zhang, (2014) in the 40s-70s latitude belt.

Total Cloud Columns Meeting MBL, Single Layer Conditions: 17,399,960			
	0-1 km	1-3	3-5
Total	0.47	0.48	0.05
Precipitating	0.08	0.67	0.97

2. Data and Methods

In this study we use data from recent voyages by Australian vessels between Hobart, Tasmania and Antarctica (Figure 1). These voyages included a similar set of remote sensing measurements that allow us to apply an identical cloud property retrieval algorithm to each campaign data set. The critical measurements include radar reflectivity (dBZ_e) profiles from vertically pointing W-Band radars, attenuated backscatter (β_{obs}) profiles from vertically pointing optical lidars, downwelling microwave brightness temperatures T_b at 31 GHz from Radiometric radiometers, and regular radiosonde soundings. Surface meteorological measurements, sea surface temperatures, and downwelling solar and infrared broadband fluxes were also collected in each campaign. Extensive aerosol measurements were also made during these campaigns. Of relevance to the present study are the cloud condensation nuclei (CCN) and sulfate aerosol observations.

The first of these voyages took place aboard the Australian Research Vessel (RV) *Investigator* in March and April of 2016 (Mace and Protat, 2018a and b, hereafter MP18a and MP18b, respectively). Unlike the other voyages, the 2016 voyage, hereafter referred to as CAPRICORN I spent its nearly 5-week duration north of 53°S and most that time near 45°S and

142°E servicing Southern Ocean Time Series buoys (Schulz et al., 2012). In total we use 137 hours of non-precipitating liquid cloud data from CAPRICORN I.

CAPRICORN II was an observational campaign also conducted on board the Australian Research Vessel (RV) I*nvestigator* during a voyage from Hobart to the Antarctic Shelf between January 11, and February 21, 2018. CAPRICORN II occurred in conjunction with the U.S. National Science Foundation-sponsored Southern Ocean Cloud Radiation Aerosol Transport Experimental Study (SOCRATES) campaign (McFarquhar et al., 2020). SOCRATES featured 15 flights by the National Center for Atmospheric Research (NCAR) Gulfstream V. CAPRICORN II included the same cloud instruments that participated in CAPRICORN I as described in MP18a. In this study we focus on data from the W-Band Doppler Cloud radar, 355 nm Lidar, and a two-channel microwave radiometer with the addition of a radar wind profiler, from the NCAR integrated sounding system. During the 7-week voyage, approximately 300 radiosondes were launched on a 3-6 hourly schedule depending upon weather.

The CAPRICORN II voyage track was mostly determined by oceanographic objectives that included some 88 preplanned stations at which conductivity, temperature, depth (CTD) and trace metal soundings of the water column were conducted. Stations were occupied along the 130° to 150° E meridians during the voyage with a delay at each station for 6-24 hours depending on oceanographic objectives. Stations were separated by an average of approximately 50 km. From an atmospheric sampling perspective, small steps with roughly half-day delays allowed for a unique characterization of the structure of cloud and thermodynamic properties of the Southern Ocean summer atmosphere. Investigator passed south of 50°S on 18 January and 60°S on 27 January both along the 140°E meridian. The southernmost point was reached on February 2 near the seasonal ice edge at 66°S. Investigator then remained south of 60°S occupying stations between 132 and 150 E until 15 February. Following the final oceanographic station occupied near 57° S and 132° E on 16 February Investigator made a brief eastward excursion to coordinate with a GV flight on 18 February near 57°S 140°E and another minor diversion to coordinate with a descending overpass of the CALIPSO satellite at 48°S and 144°E on 20 February. We use 78 hours of non-precipitating MBL clouds from CAPRICORN II.

The MARCUS campaign featured components of the U.S. Department of Energy's (DOE) Atmospheric Radiation Measurement (ARM) program's second Mobile Facility (AMF2) deployed on board the Australian ice breaker RSV Aurora Australis during the 2017-2018 Antarctic summer resupply voyages. Based out of Hobart, four voyages took place from early November, 2017 through March, 2018 (Figure 1). The key instrumentation that we use are β_{obs} from a Micropulse Lidar, Tb from a Radiometrics microwave radiometer (Liljegren, 1994; Liljegren et al. 2001), and radar reflectivity profiles from the Marine W-Band ARM Cloud Radar (M-WACR). Radiosondes were launched on a 6-hourly schedule when away from Hobart and these were supplemented by the standard ship-based meteorological and sea surface temperature measurements. Unlike the CAPRICORN voyages, the purpose of the four Aurora Australis voyages were to resupply the Australian Antarctic stations. Therefore, the ship steamed from Hobart to and from the Antarctic coast directly, while avoiding bad weather and as much of the early-season thick sea ice as possible. Each 1-way transit to and from Antarctica took from 7 to 10 days depending on destination. The ship's speed reduced in sea ice and the ship spent up to two weeks at each station for the resupply operations. The final voyage of the season to and

from Macquarie Island (55°S) occurred during the first two weeks of March. Most instruments were not operated while the ship was moored in Hobart between voyages. In total, we use 265 hours of non-precipitating cloud data from Marcus.

3. Method

We seek to examine the properties of an important genre of clouds that influence the radiative properties and cloud optical depth feedbacks in the Southern Ocean. Non-precipitating liquid clouds are ubiquitous across the Southern Ocean and compose roughly half of all clouds in the MBL (Table 1). From an analysis standpoint, the single-phase liquid and non-precipitating clouds require a minimum of assumptions in developing algorithms needed to infer their properties, thereby minimizing uncertainty. We implement an optimal estimation algorithm that derives the layer mean liquid water path (LWP), the layer mean effective radius (r_e) and the cloud droplet number concentration (N_d) using an optimal estimation (OE) algorithm that combines β_{obs}, dBZe, and Tb. Reasoning that β_{obs} constrains approximately the 2nd moment of the droplet size distribution (DSD), dBZe constrains the 6th moment of the DSD in the Rayleigh scattering regime, and Tb provides an integral constraint on the vertically integrated condensed water (LWP), the measurement combination uniquely constrains the DSD. Note that in CAPRICORN II and MARCUS, the W-Band radars were on stabilized platforms. This was not the case in CAPRICORN I. Therefore, we do not use the Doppler velocity in this study which would be an interesting addition in this cloud genre to constrain vertical motions and turbulence. Our retrieval methodology is based on the approach described in Mace and Protat (2018b). However, we will describe the algorithm in detail because of several improvements made since that initial study. Our basic assumptions, however, are largely unchanged.

To illustrate our methodology (Figure 2), we use a time section of measurements from CAPRICORN II collected on January 29 when the ship was in the vicinity of 64°S and 140°E. This day was characterized by an overcast MBL cloud layer that precipitated until late in the day. There were 8 soundings launched during this 24 hour period.

3.1 Initial Data Processing and Calibration

The lidar measurements that we use were collected from a 532 nm Micropulse Lidar for MARCUS and from a 355 nm RMAN lidar system in CAPRICORN I and II (See Royer et al. 2014 and MP18a for a brief description of the RMAN system). Both systems provide an elastic backscatter and depolarization channel. While the RMAN system does provide a Raman scattering channel, the sensitivity of the system is such that long integration times in cloud-free tropospheric air are required for calibration (Alexander and Protat, 2019). In our earlier work (MP18b) we relaxed the β_{obs} profile to theoretical Rayleigh β_{obs} profiles from clear sky nights. The calibration of the lidar, however, drifts significantly on timescales of hours resulting in large uncertainties in β_{obs} that we accounted for in our earlier work by increasing the error in β_{obs} in the OE algorithm. Here, we implement a calibration method that is particularly suitable for the clouds that we are considering using a methodology described first by O'Connor et al. (2004).

From the early work of Platt et al. (1999) and following Li et al., (2011), we express the observed attenuated backscatter as

$$\beta_{obs}(z) = \beta(z)e^{-2\int \sigma dz} \quad (1)$$

Where the measured β_{obs} is the result of 2-way attenuation through the cloud to a point z in the layer and σ is the extinction coefficient with units of inverse length where σ is expressed in terms of the lidar ratio, $S = \frac{\sigma}{\beta}$, and a factor η that accounts for the addition of photons to the observed signal due to multiple scattering in optically dense clouds allowing use to write (1)

$$\beta_{obs}(z) = \beta(z)e^{-2\eta S r} \quad (2)$$

Where we are averaging over the layer through a range r. Defining the layer-integrated total attenuated backscatter as $\gamma = \int \beta_{\parallel+\perp}$ and the layer integrated depolarization ratio as $\delta = \frac{\int \beta_{\perp}}{\int \beta_{\parallel+\perp}}$ we can express $\eta = \left(\frac{1-\delta}{1+\delta}\right)^2$ (Hu et al. 2006a,b). Platt et al. (1999) relates S with η according to $S\eta = \frac{1-T^2}{2\gamma}$ and where T is the layer transmittance. When the layer is fully attenuating (T=0) and

$$S = \frac{1}{2\eta\gamma} \quad (3).$$

O'Connor et al. (2004) and Hu et al. (2009) among others show that S varies over a narrow range in liquid water clouds with an average near 18.8. We confirmed this by examining S calculated from Mie theory using observed DSDs collected in water clouds during Rain in Clouds over the Ocean (RICO; Rauber et al., 2006). We found that S and r_e vary systematically (Mace et al. 2020), with a small dynamic range of S from 17-19 for >90% of all cloud DSDs observed during RICO. This range is small with respect to the calibration uncertainty in measured β_{obs} for elastic lidars and in the assumptions used to derive Equation 3. Following O'Connor et al. (2004) therefore, we assume that S in water clouds can be fixed at a mean value of 18.7 (the mean value we found from the RICO DSDs) that corresponds to an assumed r_e of ~10 um. We effectively calibrate the lidar signal by adjusting γ by a factor that gives S=18.7 on a profile-by-profile basis. This method of auto-calibration (O'Connor et al.'s term) then allows us to have a physically consistent characterization of β_{obs} independent of using the Rayleigh method in nighttime cloud-free skies. Application of this method to the data collected on January 29 is shown in Figure 2 where a mean factor of 3.5 is applied to the observed lidar β_{obs} on this day to achieve an S of 18.7. The limitations of this method are obvious since we implicitly make an assumption that the layer-mean effective radius is approximately 10 um. However, as we show below, the OE inversion methodology allows the final solutions to depart from this assumption.

As the lidar signal penetrates into an optically thick cloud, β_{obs} becomes increasingly dominated by multiply scattered light becoming increasingly depolarized relative to the transmitted signal and this effect is quantified by η. The 355 nm system will have a sharper forward diffraction peak than the 532 nm MPL system, resulting in less integrated backscatter and lower values of η. This weaker signal is compensated by the lower background signal in the UV channel compared to the MPL. Typically, β_{obs} increases from cloud base to a maximum value a few range bins into the layer, and β_{obs}then begins an exponential decay as it becomes increasingly dominated by multiply-scattered light. Following Li et al. (2011), If we take the

natural logarithm of both sides of equation 1, we can write $\eta\sigma = -\frac{\ln\beta_{obs} - \ln\beta}{2r}$ where the right hand side is the logarithmic decay of the multiply-scattered signal with depth. Because we have estimated η from measurements (independent of calibration), we can make a determination of σ in the optically thick part of the layer beyond the peak in β_{obs}. Li et al. (2011) compare σ derived from this method to estimates of σ derived from passive reflectance techniques and find an uncertainty of ~13%. The accuracy of this method is dependent on calculating the rate at which the signal decays with depth in the layer. In practice, we fit a regression line to β_{obs} at heights above the layer maximum in β_{obs} until the signal is a factor of 2 above the noise floor that is determined from the mean β_{obs} well above the fully attenuating cloud layer. The goodness of the linear regression fit depends on the number of measurements in this range and the accuracy is dependent on the vertical resolution of the lidar measurements when σ is large. The vertical resolution of the RMAN and MPL data during these campaigns is 15 m. We find that for clouds with σ less than 50 km^{-1} we are able to use 3-5 data points to estimate the slope. When σ becomes much larger than 75 km^{-1}, we find that typically only 2-3 points are available and the uncertainty in σ becomes large. We found this to be a limiting issue in only a few cases near the coast of Tasmania when the clouds existed within continental air masses. Figure 2 shows lidar data from a case collected on January 29. We find that on average the layer observed on January 29 had a mean σ of approximately 20 km^{-1} varying from 10 to 40 km^{-1}. This case is discussed in more detail below.

To separate liquid phase clouds from clouds that are mixed phase, we follow the approach used in MP18A where we examine the sub cloud for measurable signal depolarization. In warm clouds for CAPRICORN I and II and MARCUS after 15 January where precipitation is known to be liquid, we found that the vertically resolved sub cloud depolarization ratios were reliably less than 0.1 and in situations when the precipitation was known to be frozen, the sub cloud depolarization ratios typically exceeded 0.2. Figure 2 shows a time series of sub cloud depolarization ratios from a cloud layer with base temperature near -8°C that was producing occasional frozen precipitation at the surface noted by observers. We see pockets of ice phase precipitation from this layer but most of the precipitation observed by the radar was liquid and did not reach the surface. A known issue exists with the MARCUS MPL during the first half of the campaign (through voyage 2 that ended on 12 January) where the window through which the MPL viewed the atmosphere changed the polarization state of the laser light. This resulted in the minimum depolarization ratio measured by the instrument to be ~0.2. This issue was corrected in Hobart on 15 January 2018 prior to voyage 3. Since we found that when ice was present near cloud base, the depolarization ratios typically exceeded 0.4, we use a threshold of 0.3 for the early MARCUS voyages to identify the presence of ice while for later MARCUS and CAPRICORN I and II, we use a sub cloud depolarization ratio of 0.25 as a threshold.

The vertically pointing millimeter radars used in CAPRICORN I and II and MARCUS were W-Band Doppler systems. In CAPRICORN I and II the radars used were the Bistatic Radar System for Atmospheric Studies (BASTA; Delanoë et al., 2016). The BASTA radar observations were calibrated using statistical comparisons between BASTA, the Ku-band micro rain radar, and Ku-band and W-band T-matrix calculations using the ODM470 disdrometer observations from the mast (see Klepp et al. 2018 for more details and CAPRICORN I results). BASTA cloud

radar observations from ground-based deployments surrounding the CAPRICORN experiments were also compared statistically with CloudSat reflectivities using the technique outlined in Protat et al. (2011), confirming the calibration figures derived from the disdrometer and micro rain radar comparisons (not shown).

As noted recently by Kollias et al., (2019), the ARM millimeter radars are subject to significant calibration uncertainties. Specifically, Kollias et al, (2019) compared the M-WACR measurements with CloudSat and noted that the M-WACR calibration ranges from 4 to 8 dB lower than the well-calibrated W-Band radar on CloudSat (Tanelli et al., 2008). Such a calibration uncertainty is prohibitive for quantitative use of the radar reflectivities, and no direct means of calibrating the M-WACR system were available during MARCUS. Furthermore, during late 2017 and early 2018, CloudSat was involved in a transition in orbit so regular data were not collected. In order to establish some means of assessing the calibration of the M-WACR, we reason that the RSV Aurora Australis and the RV Investigator were collecting data in a similar region during a common period of time and aspects of their data should, therefore, be similar. In particular, with both BASTA and M-WACR operating near 94 GHz, we would expect that the radar reflectivity statistics of the sub-cloud base liquid precipitation observed during their common sea time (January and February) and common latitude range (north of 66S) should be similar. We therefore examine the radar reflectivity statistics in the 200 m above the radars and up to 1 range bin below the lidar cloud base (to a maximum height of 1 km) when the lidar depolarization ratios below a measured cloud base indicated the presence of liquid hydrometeors and the BASTA dBZe recorded values in excess of -20 dBZe. The results are shown in Figure 3. We find that the M-WACR is indeed offset low from the results measured by the calibrated BASTA radar during CAPRICORN II. Adding 4.5 dB to the M-WACR sub-cloud precipitation results causes the two histograms to come into alignment (Figure 3 shows the uncorrected MARCUS results). This offset is consistent with the findings of Kollias et al (2019) and therefore, in all results presented henceforth this offset will be added to the M-WACR dBZe measurements.

3.2 Algorithm to Derive N_d, LWP, and r_e

The non-precipitating liquid phase clouds that we examine are assumed to be composed of a single mode of droplets that can be described by a modified gamma distribution,

$$N(D) = N_0 \left(\frac{D}{D_0}\right)^{\alpha} exp\left(-\frac{D}{D_0}\right) \quad (3)$$

Where N(D) is the droplet number per unit size and has units of cm^{-4}. N_0, D_0, and α are characteristic number, diameter and the shape parameter of the DSD. All units are cgs unless specified otherwise. This simple integrable function allows us to express the microphysical quantities, N_d (cloud droplet number), q (liquid water content), and r_e (effective radius) with the following expressions,

$$N_d = N_0 D_0 \Gamma(\alpha + 1)$$

$$q = \rho \frac{\pi}{6} N_0 D_0^4 \, \Gamma(\alpha + 4) \quad (4)$$

$$r_e = \frac{D_0}{2} (\alpha + 3)$$

Where we have used the recursion properties of the gamma function in the ratio of the third and second moments of N(D) for r_e. See Posselt and Mace (2014, their appendix B). Similarly, we can relate observable quantities to N(D) using the appropriate moments. The radar reflectivity parameter, Ze, can be written as the sixth moment of N(D)

$$Z_e = 10^{12} N_0 D_0^7 \Gamma(\alpha + 7) = 10^{12} \frac{48}{\pi} r_e^3 q F_6. \quad (5)$$

Where the constant 10^{12} converts from cgs to the typical units for Z_e of mm^6 m^{-3} and $F_6 = \frac{(\alpha+6)(\alpha+5)(\alpha+4)}{(\alpha+3)^3}$ arises from the recursion properties of the gamma function. Equation 5 assumes that the droplets remain small with respect to the wavelength of the radars (~3mm) so that the Rayleigh approximation is valid. The lidar backscatter and extinction coefficients are similarly derived from second moments of N(D) times $\frac{\pi}{4}$ multiplied by the extinction efficiency (here assumed to be 2) and the backscatter efficiency which is assumed constant at 0.12 (MP18b), respectively (see Posselt and Mace, 2014).

The OE inversion methodology is convenient for arriving at solutions to problems using disparate data streams that account for uncertainties in observations and assumptions given prior statistics (Maahn et al., 2020; Mace et al., 2016). The method we use is adapted from Rogers et al (2000) and minimizes a cost function using Gaussian statistics and Newtonian iteration. In a problem with several degrees of freedom and inherent uncertainties in observations and forward models, it is often necessary to begin the iteration with a physically reasonable first guess to avoid converging on an unphysical local minimum of the cost function generated by uncertainties. To arrive at this first guess, we combine Z_e, σ derived from β_{obs} and Tb. We use a simplified analytical model relating Tb and LWP (MP18b),

$$\delta T_b = T_{eff}\left(1 - exp\left(-\frac{3}{2} a_b LWP\right)\right) \quad (6)$$

Where δT_b is the increase in 31 GHz Tb caused by the presence of the cloud layer and $a_b = 1.712$ is the mass absorption coefficient in cgs units (MP18b). The measurements then constrain the mass and the cross-sectional area of what we assume to be a layer-mean DSD. We then iterate to estimate α using Z_e as a constraint. Reasonably often, however, the W-Band radars do not detect the non-precipitating cloud layers. This occurs approximately 25% of the time for CAPRICORN I and II and 15% of the time during MARCUS (we estimate the M-WACR was ~5 dB more sensitive than the BASTA radars). In such cases we fix our initial estimate of α at a mean value of 2.5 derived from in situ data collected during SOCRATES. This first guess N(D) is then used to begin the OE iteration.

The OE algorithm that we employ is identical to that described in MP18b starting at equation 12 of that paper with all observations interpolated to the time indexes of the BASTA radar. The main difference between the earlier work and here is that the β_{obs} measurements are calibrated using the method described earlier and the first guess is constrained by the extinction coefficient derived from the lidar data. Because we start with a microphysical estimate that already reasonably replicates the measurements, the final solution does not depart substantially from the first guess. Therefore, the constraints provided by the lidar-derived extinction are a critical new feature of this updated approach. Another important difference between MP18b and this analysis is that we use prior statistics derived from the in-situ data collected during SOCRATES (Wang et al., 2020). Therefore, the algorithm produces results that are statistically similar to this specific prior knowledge of SO clouds. We also focus

on N_d in this study. While we do not retrieve N_d specifically, we derive it from the retrieved LWP, r_e, and α. We use the uncertainties of the retrieved quantities with a bootstrap approach (Kirk and Stumpf, 2009) to estimate the uncertainty in N_d. This is discussed in more detail below where we explain and demonstrate uncertainty and validation of the algorithm. We also use solar flux radiative closure as a means of validation. This is discussed in more detail in the following sections.

4. Results

4.1 January 29 CAPRICORN II Case Study

During the latter of half the UTC day on 29 January 2018 the R/V Investigator was stationary near 63.5°S and 139.8°E in the cold sector of a deep cyclone that had passed early during the UTC day on 28 January. On 29 January the low pressure was centered near 65°S and 170°E. At the R/V Investigator location, surface temperatures were just below freezing during much of the day on 29 January and occasional light snow grains were reported from an overcast stratocumulus layer by radiosonde operators during 3-hourly launches. Winds were sustained southerly around 20 knots and surface pressures rose steadily from a minimum of 965 mb early on 28 January to 985 mb at 18 UTC to 990 mb by 00 UTC on 30 January. Figure 2a and b show that at 15 UTC on 29 January the cloud layer base was near 750 m and the radar layer tops extended to ~1.5 km. The BASTA w-Band radar observed occasional light precipitation from this overcast layer and Lidar depolarization ratios suggest that the sub cloud precipitation was mostly liquid with pockets of ice phase typically associated with peaks in the radar reflectivities but not always. The MRR recorded light precipitation during several brief periods (less than a few minutes in duration) prior to 12 UTC on 29 January but none after 12 UTC and no precipitation was recorded by the ship rain gauge suggesting that the precipitation was very light. The sounding at 1600 UTC (not shown) indicates that the lifting condensation level (LCL) was near cloud base at -8°C with a marine inversion base near 1.3 km at -14°C and inversion top near 1.45 km. The 1600 UTC sounding indicates that the MBL was well mixed from the surface to cloud base. After 1600 UTC, the light precipitation observed by the W-Band radar became lighter and less frequent and after 18 UTC, the radar reflectivity of the layer fell below the detection threshold of the W-Band although the cloud layer was persistent through 21 UTC according to the lidar and microwave radiometer. Lidar-derived extinctions in this layer were steady between 30 and 40 km^{-1}. This layer was well characterized by the RMAN lidar with uncertainties in the extinction in the range of 20-30%.

As the precipitation mostly ceased after 16 UTC, we are able to derive cloud properties from the remote sensing data in the supercooled liquid cloud layer using the method described above. In the hour between 16 and 17 UTC, water paths were steady between 200 and 300 g m^{-2} (Fig. 2e) with uncertainties near 15%, effective radii were variable but averaged 12 μm (Fig. 2f) with uncertainties in the 10% range and Nd was mostly below 50 cm^{-3} (Fig. 2g) with uncertainties of approximately 70-80%. As the precipitation ceased and the radar reflectivity decreased to below the detection threshold of the BASTA w-band, the water path of the layer gradually decreased and became variable (Fig. 2e). Note that as the reflectivity dropped below the BASTA detection threshold, the uncertainty of r_e and N_d increases. This is the result of how

we handle the OE inversion when the radar is unable to sense the layer. Because we know the radar detection threshold, we know that the maximum radar reflectivity in the layer must be lower than that threshold. Therefore, we set the radar reflectivity to -35 dBZe and assume that the uncertainty in that reflectivity is 5 dB. This allows us to use the measurements of LWP and σ and use the knowledge that the dBZe is lower than the detection threshold. The uncertainties in r_e, then increase to be typically on the order of 50% and the uncertainties in N_d increase to ~120%.

An interesting aspect of this case study is that before the layer became completely undetectable by the w-band, r_e and N_d begin opposite trends with N_d increasing and r_e decreasing. This change begins near 17:10 UTC and by 17:30 UTC r_e is steady near 8 um while N_d effectively doubles to be in the 100 cm^{-3} range. These changes then persist through the remainder of the period even when the layer is observable by radar at a few instances. We note this because we see an associated change in aerosol properties and chemical composition recorded at the surface about an hour after the change in the cloud layer (Figure 2h). CCN at 0.55% super saturation increases from ~150 cm^{-3} to 300 cm^{-3} and the sulfate mass concentration in submicron aerosol increases from 0.2 to 0.5 $\mu g/m^3$ as measured by the Time of Flight Aerosol Chemical Speciation Monitor (Tof-ACSM; Fröhlich et al, 2013).. The step increases in aerosol properties are consistent with increased N_d and decreased r_e. We note that LWP becomes variable and decreases but does not seem to be responding in a similar stepwise fashion as do r_e and N_d. The lidar data and associated derived products do not demonstrate an abrupt transition at this time. We do note that over the period shown in Figure 2 the cloud base as derived from lidar β_{obs}lifted gradually and evidence for sub cloud precipitation became more sparse. A careful examination of the δ and η also demonstrate a gradual increase and decrease, respectively, between 11 and 20 UTC. This would be consistent with droplets becoming smaller and N_d increasing although σ remains near 20 km^{-1} through the period.

The ~1 hour time offset in changes between the surface aerosol and cloud layer is curious. Recall that the 16 UTC sounding showed the MBL to be well mixed. However, a sounding launched at 19 UTC showed that the inversion base had descended to 1.2 km (top remained near 1.4 km) and the surface layer was decoupled from the deeper MBL by a weak inversion at 200 m. Below 200 m height, the humidity was largely unchanged while above 200 m the profile had dried considerably in the intervening three hours likely explaining the decrease in LWP. It is plausible that free tropospheric air containing biogenic sulfate aerosol had mixed into the MBL reducing humidity and influencing cloud properties. Because the MBL was decoupled, it took some time for that change to be mixed to the surface.

We further note that this step change in aerosol chemistry and CCN is similar to events described by Humphries et al. (2016) at similar latitudes and times of year. Up to this time during CAPRICORN II, sulfate concentrations had remained mostly below 0.2 ug m^{-3} and the step change on 29 January to values in excess of 0.4 ug m^{-3} marked the beginning of elevated surface CCN and sulfate that persisted until 4 February while the ship operated south of 65 S. Markers of continental air mass origin such as radon were absent during this period, however this may not be expected if air masses originated from the ice-coved Antarctic continent. Cloud droplet numbers during this time remained mostly elevated in excess of ~100 cm^{-3} until 4 February when extended poor weather precluded cloud retrievals until 15 February. See

McFarquhar et al. (2020) their figure 3 for a daily summary of CAPRICORN II cloud and aerosol time series that illustrate these events.

4.2 Cloud Properties

One of the key motivating factors for the SO measurement campaigns is the surface solar radiation bias common to many climate models. However, actual measurements of surface solar radiation and associated clouds are rare in the SO. Here, we explore the properties of a genre of clouds that are key components of the surface energy balance of this region. We combine data from the MARCUS and CAPRICORN campaigns into a single data set that brackets the Austral Summer months from November through mid-April and ranges in latitude from the East Antarctic coast where the Aurora Australis spent several weeks of its campaign to the latitude of Hobart near 42°S that was the common home port for both vessels. In total, we consider 480 hours of retrieved cloud properties. We find that the non-precipitating clouds in this region during the warm season are composed of layers with LWP in the range of 90 g m^{-2} with a standard deviation of about 100 g m^{-2}, r_e near 8.7 μm +/- 3 μm, and N_d near 90 cm^{-3} with about a 200% standard deviation (Figure 4). In Figures 4b and 4c, we compare the retrieved values with distributions derived from the SOCRATES in situ microphysical measurements where we exclude the precipitation mode in bimodal liquid droplet distributions (Mace et al., 2016). We have also compared q by dividing the retrieved LWP by the layer thickness with the q measured in situ and found similarly unbiased agreement (not shown). The offset that we see in the in situ and retrieved N_d distributions is expected because the larger N_d values in the retrievals are derived from cases near Antarctica and also close to Tasmania where SOCRATES did not sample (see McFarquhar et al., 2020 and below). We note that the retrieved cloud properties are in broad agreement with similar quantities derived from A-Train data (Mace and Avey, 2017; McCoy et al., 2015) where they demonstrate that the microphysical properties of these clouds vary seasonally with higher N_d and lower r_e during summer than winter associated with changes in aerosol derived from biogenic sources. Because the A-Train is limited to layers above 1 km in altitude, we report here generally lower water paths than in Mace and Avey (2017).

In Figure 4 we also show the uncertainty statistics in the retrieved microphysical quantities. Consistent with our discussion of the case study in Figure 2, we find that LWP and r_e are retrieved typically to within a few tens of percent while N_d is not known to within a factor of 2 generally. The high uncertainty in N_d is expected. Being the zeroth moment of the DSD, N_d is not directly constrained by any of the remote sensing measurements. β_{obs} being a function of the 2nd moment of the DSD comes closest but even β_{obs} is still two orders removed meaning that the droplet sizes in the DSD that control N_d are typically not those that control the cross sectional area and β_{obs} Constraining cross sectional area simply does not constrain N_d without additional assumptions regarding correlations among the DSD moments. We, therefore, rely on the correlations among the microphysical quantities to derive N_d. The natural variability in the covariances that exist in the prior data combined with uncertainties in the retrieved quantities drive the resulting uncertainty in N_d that is shown in Figure 4.

We use solar radiation measured at the surface as a means of vicarious validation of the retrieved microphysics. Following the method described in Berry et al., (2019 and 2020), we

calculate the downwelling solar flux at the surface using the two-stream radiative transfer model described by Toon et al. (1989) as modified by Kato et al. (2001). For solar zenith angles less than 80° with no higher cloud layers, we compare the downwelling solar fluxes measured on the ships with those calculated using the retrieved microphysical quantities. There are challenges with such an approach since we are measuring the cloud properties at zenith and then assuming that those properties are spread over a plane parallel sky. Our assumption is that any significant biases in our retrievals would show up as overall biases in the solar flux comparison. Using this method, we found extended periods when the flux was clearly biased high or low over periods of hours. This caused us to remove 3 cases from the CAPRICORN I data, 6 cases days from the CAPRICORN II data, and 4 case days from the MARCUS data set due to large biases in fluxes. In most of these poorly rendered cases it seems that the MWR or radar radome or both were wetted by precipitation or sea spray and/or the lidar window was covered by condensed sea salt – operating sensitive instrumentation at sea in the Southern Ocean is challenging. We conducted this manual filtering on daily timescales. If a day appeared on average reasonably unbiased, we kept that day in the data set. What we find after removing obviously bad days is that the flux difference (calculated flux minus observed flux) has a modal value at -4 W m^{-2} with a mean, median and standard deviation of 25, 18, and 63 W m^{-2} respectively (Fig. 4g). Because the low-level clouds are typically cellular even when overcast and allow for variable transmission of sunlight and three dimensional radiative effects, it is not unexpected that the bias is negative at higher values of flux. This is indicative of direct beam sunlight reaching the pyranometers at higher zenith angles and/or reflection from cloud sides. See also the negative solar forcing in the red histogram derived from the observed fluxes in Figure 4h as evidence of these 3d effects. While our goal is to show an unbiased comparison, the distribution in Figure 4g has a -6% bias suggesting that the retrieved microphysical properties are physically reasonable but with possible low (high) biases in LWP (r_e) or offsetting biases in both that are unknown. Unfortunately, no airborne validation is available. While the NCAR GV aircraft flew over the R/V Investigator several times during CAPRICORN II, these instances occurred when the MWR was wet due to drizzle or sea spray and retrievals could not be conducted.

As discussed in Protat et al. (2017), MBL clouds like those considered here have a significant impact on the downwelling solar flux at the surface (Figure 4h) and top of atmosphere (TOA, Figure 4i). Expressing the net solar cloud radiative effect (CRE) as one minus the fraction of the downwelling cloudy flux divided by the clear sky solar flux, we find a mean value of 0.52 with a standard deviation of 0.33. The effect of these clouds then is to remove typically between 1/3 and 2/3 of the solar radiation from the net surface fluxes when they are present. The solar forcing derived from the actual flux observations (normalized by the calculated clear sky), shows a broader distribution that extends to negative values indicating reflection from cloud sides but also reflection from and blocking of sunlight by the ship super structure.

The effect of these clouds on the solar energy balance is realized at the TOA by albedos (A) that average 0.47 with a standard deviation of 0.12. A question we address below in more detail is the extent to which the radiative effects of these clouds are susceptible to changes in microphysics. The scatter plot of A versus optical depth shows that the majority of these clouds exist at optical depths that are lower than ~20. For comparison, Painemal and Minnis (2012)

examine data from eastern ocean basin stratocumulus using geostationary data and find significantly lower A (0.2-0.3) from lower LWP (~60 g m-2) and higher N_d (150-200 cm^{-3}). The analysis of Abel et al (2010) of the SE Pacific stratocumulus data show that N_d tended to decrease away from the coastal regions to values near 100 cm^{-3} while water paths also increased to values in excess of 150 g m^{-2}. Lu et al. (2009) analyzing airborne stratocumulus data offshore of California showed a similar tendency with lower N_d and larger r_e with distance from the continental influences.

Additional understanding of the Southern Ocean clouds, the processes involved in their maintenance, and the effects they impose on the energy balance can be gained by examining relationships among the variables – in particular how the microphysics and radiative effects are interrelated. This thinking has heritage back to at least Twomey (1977) who showed fundamental dependencies of A on N_d, i.e. the Twomey Effect. Because A is a function of both the amount of condensed water in the column and how that water is distributed into the DSD, the relationships are not necessarily straightforward. Often microphysics derived from satellite use absorbing and non-absorbing solar channels to retrieve optical depth and r_e with water path derived from perhaps coaligned microwave radiometer measurements and N_d is further derived from assumptions. Our observations are of higher spatial resolution with the LWP constrained by the microwave radiometer, the cross-sectional area of the DSD constrained by the lidar, and the droplet sizes constrained by the radar. While there are still significant uncertainties in the results, these unique measurements combined with coincident aerosol measurements allow us to explore the role of these clouds in the SO atmosphere and surface energy balance.

Recently Gryspeerdt et al. (2019) examined global MODIS retrievals and found, in agreement with previous studies, that cloud LWP is nonmonotonically related to N_d with LWP increasing for lower N_d due to precipitation suppression while at higher N_d, more rapid evaporation with smaller r_e tends to cause water path to decrease with N_d. While our data excludes precipitation, we do not control for the nearby presence of drizzle or snow. In other words, the non-precipitating clouds we analyze could be associated with nearby precipitation and their properties modulated by precipitation processes. In Figure 5b we plot the relationship of LWP as a function of N_d and we color code the scatter plot by r_e as described in the caption. There is a strong relationship between N_d and LWP for a given r_e with LWP increasing with r_e for a given N_d but there is some range (i.e. freedom) for LWP to vary for a given N_d, r_e pair. We note that this scatter plot looks nothing like those shown in Gryspeerdt et al. (2019) except that by binning the LWP as a function of N_d and then plotting the median value of that LWP, we also find a relationship where LWP tends to increase with N_d until about 100 cm^{-3} when the tendency is for LWP to begin decreasing with N_d. The inflection point in N_d that we find is larger than in Gryspeerdt et al. (2019) but we can perhaps interpret the results similarly. Mace and Avey (2017) found similar effects on a seasonal basis with A-Train where a given precipitation rate required higher LWP at larger N_d.

While it seems that the LWP can be modulated by the properties of the DSD, it is the LWP that largely controls the effect of the clouds on the energy budget through A and surface solar effect. This property is illustrated in Figure 5c and d where we plot A as a function of N_d and visible optical depth τ with the LWP color coded as in Figure 5b and r_e color coded in Figure 5c. A increases with water path while the smaller r_e clouds tend to be associated with the

higher optical depths and larger *A*. Simply linearly regressing *A* as a function of N_d in the LWP ranges for the colored points in Figure 5b, we find that within a given LWP range, *A* tends to increase as N_d increases because increasing N_d is associated with decreasing r_e – although the primary factor in determining *A* remains the LWP. The positive slopes on these regression curves have been studied as the albedo susceptibility (Platnick and Twomey, 1994). Painemal and Minnis (2012) define the albedo susceptibility $S_R = \frac{dA}{dlnN_d}$ and it is determined using the linear regression slope A with N_d within LWP bins as in Figure 5b. S_R is plotted for the SO liquid phase clouds in Figure 5a. We find values of S_R that are generally smaller than those found by Painemal and Minnis (2012) in the marine stratocumulus regions. Approximately 90% of our data have LWP greater than 20 g m^{-2} and less than about 250 g m^{-2}. Therefore, results outside that range should be viewed with appropriate skepticism. At its maximum near 0.045 (0.055 in the Southern region), the value of S_R implies that a doubling of Nd would result in about a 0.9% (1.1%) increase in *A*. Painemal and Minnis (2012) find a similar pattern with a tendency for S_R to have a maximum at approximately 50 g m^{-2} and then decrease towards larger LWP although the decrease of S_R in the southern region is larger than in the more northern latitudes and reaches a minimum at lower LWP. The decrease of S_R with LWP can be understood by considering that the reflectance of a cloud layer tends to asymptote to a maximum value as the optical depth increases beyond about 20. So, as the layer becomes optically thicker due to higher LWP, the ability for the microphysics to influence *A* lessens and thus S_R decreases. These results suggest that the Southern latitude domain reaches this saturation point at smaller LWP meaning that the clouds A is less susceptible to microphysics overall. The 95% confidence intervals in the regression slopes plotted on the figure show significant uncertainty especially in the southern region. However, the systematic nature of the tendency of SR with LWP provides additional confidence in the overall results.

4.3 Latitudinal Variations

Based on the physical oceanography (i.e. Armour et al., 2016) and biology (e. g. Deppler and Davidson, 2017; Krüger and Graßl, 2011; McCoy et al, 2015) of the SO, we further explore the latitudinal variability in the combined liquid cloud data set. A convenient set of boundaries that we impose is based on Deppler and Davidson (2017; their Figure 2) that shows clear variations in Chlorophyll a in the longitudinal domain we consider. From the latitude of Hobart to roughly 50°S, the ocean tends to have higher biological productivity and more quiescent weather during the summer months. The sub Antarctic front near 50°S marks entry into the Antarctic Circumpolar Current (ACC) and seasonal storm track with the climatological position of the Sub Antarctic Circumpolar Current Front near 62.5°S at this longitude marking entry into the Antarctic marginal seas. We will refer to these latitude bins as the northern (Hobart to 50°S), middle (50°S to 62.5°S), and southern (poleward of 62.5°S) analysis regions. Figure 6 summarizes the cloud and radiative properties of the non-precipitating liquid clouds observed in these regions. Recall that the step increase in sulfate aerosol concentration and CCN and N_d in the 29 January case study (Figure 2) occurred near 64°S.

The differences in cloud properties between the northern and middle regions are subtle. Overall, we find somewhat higher LWP in the middle region compared to the northern region, with two modes in the LWP distribution, the peak of the second mode corresponding well with that of the southern region. While the modal values of the N_d and r_e distributions of the northern and middle domains are similar, the N_d distribution of the middle domain is skewed to smaller values and the r_e distribution is skewed to slightly higher values. While we do not show it here in detail, these differences tend to be associated with cases collected during CAPRICORN II early in the program close to Tasmania. During CAPRICORN I, several days early in that program near 45°S had trajectories from the Australian continent, high aerosol and CCN number concentrations and larger (smaller) N_d (r_e). Proximity to Australia influences the aerosol properties of the northern domain. Also during CAPRICORN II the anomalously high SST in the Tasman sea was associated with persistently hazy conditions and higher aerosol numbers that largely returned to lower values over the middle latitude domain.

Of interest is the bimodal nature of the N_d and r_e distributions in the southern latitude domain. The overall LWP distribution is skewed to larger values (Figure 6a). One of the modes in the N_d and r_e southern domain's distributions is clearly very similar to the modal values in the two more northerly domains. A second mode tends to have significantly higher N_d and much lower r_e values more indicative of the latter portion of the January 29 case when sulfate aerosol concentrations and CCN increased and cloud properties changed. In Figure 7, we show cloud and radiation properties compiled from the period 2- 5 January 2018 when RSV Aurora Australis was at Casey Station near 66°S and 110°E. There are 4050 30-second retrievals in these distributions. We plot the in-situ distributions like in Figure 4 for reference to show how much of a contrast these clouds presented to what was measured by the SOCRATES aircraft flights. The LWP during this event was higher than average, in the 200-300 g m^{-2} range, while the N_d was often in excess of 300 cm^{-3} with r_e around 5 μm. Comparing our calculation of the downwelling solar flux with the observations shows a distribution with a strong mode near zero difference with a skew toward positive values indicating a bias in the high Nd tail of the distribution. However, with a solar noon clear sky flux near 800 W m^{-2}, the total solar forcing on this day was on the order of 500 W m^{-2} suggesting that on average our estimates of the cloud microphysics were within the uncertainties discussed earlier. Thus, we find evidence for strong bimodality in cloud properties along the coast of East Antarctica where one mode has the properties of marine clouds from farther north while another mode has quite high droplet numbers more consistent with high CCN air. The high LWP of these events strongly imply that suppression of precipitation was occurring in the high N_d droplet mode clouds.

4.4 Optical Depth-Temperature Response

As discussed recently in Terai et al. (2019; hereafter T19), there is a robust prediction among climate models that middle and high latitude clouds will impose a negative feedback on the climate system because these clouds will increase in optical thickness with warming thereby becoming more reflective. T19 comprehensively describe a number of possible physical mechanisms operating in middle latitude clouds that could cause them to either thicken or thin with warming. These mechanisms include a phase feedback where ice precipitation would decrease in tendency thereby causing clouds to have high liquid water paths and longer

lifetimes, a thickening due to the fact that the moist adiabatic lapse rate steepens with warming, or due to increased inversion strengths. Mechanisms that cause clouds to thin with increased temperature would occur due to more efficient cloud top drying or due to decoupling of the boundary layer, allowing entrainment of dry free tropospheric air to erode the cloud water path. All or most of these mechanisms are physically plausible and could work together or counter to each other to form a net response. T19 examine ground-based measurements from several middle and high latitude sites and find that the mechanisms that cause overall thinning of clouds with warming are predominant. Huang et al. (2016) examine MODIS data over the SO and find a measurable decline in cloud optical depth with increasing SST due mostly to a decrease in LWP associated with a decrease in cloud top height.

Shown in Figure 8, we find a negative trend of -0.62 K^{-1} in cloud optical depth with temperature. While the correlation coefficient is fairly weak at -0.18, the tendency for the optical depth to decrease with temperature is in agreement with T19 and Huang et al. (2016). We found a margin of error at the 99% confidence level of 0.06 K^{-1} in the regression slope using a standard methodology (Giles et al., 1988). For verification, we randomly removed half of the ~70,000 measurements and recalculating the slope 1000 times reasonably replicating the confidence interval of 0.06 K^{-1}. We find that the slope of this regression line results in a decrease in optical depth of approximately a factor two over the temperature range of the observations (255-285 K). The scatter and resulting low correlation in this relationship is not unexpected given the highly varied meteorology and differences in background aerosol over a seasonal cycle. That we see any coherent trend at all is remarkable. We examined the factors that influence the optical depth and found no significant tendencies in r_e or N_d but the LWP had a downward trend but with weaker statistical significance that seemed to be associated with a decrease in cloud physical thickness over the temperature range considered. These results are consistent with the findings of Huang et al. (2016). We consider these results to be also consistent with the finding of T19 suggesting that enhanced drying within the cloud layer is dominating other mechanisms although the data set is only marginally adequate in terms of duration to address the underlying causal mechanisms of this finding. While we are not necessarily suggesting that these results should be taken to confirm or negate a feedback response, the results do point to such mechanisms at work in this region to modulate cloud properties.

5. Summary and Conclusions

We have presented an analysis of data compiled over three ship-based field campaigns in the Southern Ocean between East Antarctica and Hobart, Tasmania. The data were collected aboard the Australian Research Vessels Investigator (CAPRICORN I and II) and RSV Aurora Australis (MARCUS). The MARCUS program ran during the summer resupply of Casey, Davis, Mawson, and Macquarie Island stations between November, 2017 and March 2018. The CAPRICORN II campaign took place in conjunction with the NSF-funded SOCRATES aircraft mission and was conducted over a six-week period from early January 2018 until late February 2018. The CAPRICORN I campaign took place in March and April, 2016 and was previously reported on by Mace and Protat (2018a and b).

We examine the properties of non-precipitating liquid phase clouds. This genre of clouds comprises nearly half of the MBL-based layers in the Southern Ocean between 40°S and 65°S based on analysis of satellite radar and lidar data (Table 1). Combining the observations from the three measurement campaigns provides 480 hours of measurements in these clouds. In addition to surface meteorology, radiation, and radiosonde soundings, the critical measurements from the three campaigns that we use to characterize cloud properties consist of zenith pointing W-Band radar, elastic lidar attenuated backscatter operating in the visible during MARCUS and in the UV during CAPRICORN, and zenith viewing microwave brightness temperatures at 31 GHz. Together, these measurements allow us to constrain the LWP, effective radius (r_e) and cloud droplet number concentration N_d of the liquid non precipitating clouds using an optimal estimation algorithm that uses prior information from aircraft data collected during the SOCRATES campaign. Uncertainties in the retrieved quantities are within 20% for the LWP. Nd is much more difficult to constrain because it is the zeroth moment of the droplet size distribution whereas the measurements tend to constrain higher order moments. Uncertainties in r_e and N_d are typically 10% and 70% depending on whether the clouds have measurable radar reflectivity since often the non-precipitating clouds fall below the detection thresholds of the radars (~25% of the time during CAPRICORN and 12% of the time during Marcus). In such circumstances the uncertainties in r_e rise to 50% and N_d to 120%.

Overall, the non-precipitating clouds that we examine over the summertime SO tend to have LWP in the 100-200 g m^{-2} , re of 8.7 um and Nd near (90 cm-3) on average making the SO clouds somewhat thicker with smaller re and higher Nd than their counterparts in the subtropical stratocumulus regions. The cloud properties drive visible optical depths of between 20 and 30 with a mean of 27 that tend to remove on average approximately ½ of the downwelling solar flux from what would occur at the surface with albedos typically near 0.5. The clouds, while typically overcast in coverage, have significant structure horizontally and result in 3D radiative effects that cause the surface flux to vary substantially.

Many of the characteristics we find in the SO clouds have also been reported in stratocumulus clouds with subtle differences. For instance, we find that higher N_d clouds tend to be associated with higher LWP values up to N_d of ~110 cm^{-3} beyond which the mean water paths tend to decrease. Gryspeerdt et al. (2019) associate this behavior with suppression of precipitation – a process that Mace and Avey (2017) documented in SO clouds between summer and winter. We also find that the tendency for albedo to be modulated by N_d is somewhat smaller for the non-precipitating clouds over the SO than for similar clouds in the eastern subtropical oceans because the clouds are generally thicker. We do find that the albedo susceptibility decreases as the LWP increases to about 200 g m^{-2} in agreement with other studies (Painemal and Minnis, 2012) for subtropical stratocumulus. The clouds over the SO also tend to have an optical depth response to temperature that is similar to findings reported from Northern Hemisphere ground sites by Terai et al. (2019) and for SO clouds analyzed from satellite by Huang et al. (2016) where the clouds tend to decrease in optical depth with temperature by about 2% per Kelvin. While there is considerable scatter in this relationship due to the underlying natural variability, these results have reasonable statistical significance and seem to be due to a thinning of the geometrical cloud layer thickness with temperature.

Perhaps most significantly, we find a bimodality in cloud properties along the coast of East Antarctica with one cloud property mode exhibiting properties consistent with the maritime clouds observed farther north. The other mode has much higher N_d, small r_e that, through precipitation suppression, allow for higher LWP to be maintained along with a concomitant increase in albedo and surface solar forcing. We document a transition in this regime with a case study from CAPRICORN II on 29 January 2018 when cloud r_e and N_d simultaneously decreased and increased substantially over the space of ~30 minutes. This change was followed by a step change in the sulfate aerosol concentrations and CCN measured at the surface one hour later. Compositional markers for continental aerosol were not observed, indicating that these were pristine air masses not altered by land emissions. Following this step change, the non-precipitating clouds retained these properties for approximately 5 days while the aerosol number concentrations remained mostly elevated. Another case at Casey station of very high N_d and small r_e clouds that persisted for several days is also shown. While additional study is needed, this variability is consistent with there being distinct air mass changes along the East-Antarctic coast associated with air that contains significantly different aerosol characteristics. Such variability in aerosol has been documented in previous field data by Humphries et al., (2016).

This work raises many questions regarding the properties and processes that modulate cloudiness in the Southern Ocean. That we see such remarkable sensitivity of this cloud genre to step changes in the background aerosol suggests that there is much to learn regarding aerosol-cloud-precipitation interactions (ACI) by studying the air mass transitions that seem to happen in this region. From a climatological standpoint, these results raise questions about the role of biogenic aerosol modulating the seasonal aerosol background state of the entire SO (McCoy et al., 2015; Mace and Avey, 2017). To what extent is the increase in summertime N_d over the wider SO caused by the massive biological phytoplankton blooms concentrated along the marginal seas of Antarctica (Shaw, 1987) or is there a general increase in biogenic aerosol throughout the broader SO? Our data are limited by bracketing a summer season. What happens, for instance, during fall as the biogenic emissions subside, and when during spring do biogenic aerosol sources begin to impact cloud and precipitation properties? Is this transition related to biogeochemical cycling of sulfur compounds in melting sea ice (Damm et al., 2016)? It is well documented that the Southern Ocean is undergoing substantial changes with climate change (Armour et al., 2016; Kennicut et al., 2014; Liu et al., 2018) and understanding the implications of these changes require documentation and understanding of the processes occurring in the high latitude regions of the SO.

Acknowledgements:

This research was supported in part by BER Award DE-SC0018995 (GM and RH) and NASA grants 80NSSC19K1251 (GM). *This project received grant funding from the Australian Government as part of the Antarctic Science Collaboration Initiative program. The Australian Antarctic Program Partnership is led by the University of Tasmania, and includes the Australian Antarctic Division, CSIRO Oceans and Atmosphere, Geoscience Australia, the Bureau of Meteorology, the Tasmanian State Government and Australia's Integrated Marine Observing System. (AP, SA, and RH)* Technical, logistical, and ship support for MARCUS were provided by the Australian Antarctic Division through Australia Antarctic Science projects 4292

and 4387 and we thank Steven Whiteside, Lloyd Symonds, Rick van den Enden, Peter de Vries, Chris Young and Chris Richards for assistance. The authors would like to thank the staff of the Marine National Facility for providing the infrastructure and logistical and financial support for the voyages of the RV Investigator. Funding for these voyages was provided by the Australian Government and the U.S. Department of Energy. All data used in this study are available in public archives. MARCUS data are available from the DOE ARM archive at https://adc.arm.gov/armlogin/login.jsp, SOCRATES data are available at https://data.eol.ucar.edu/project/SOCRATES, CAPRICORN I and II data are available at https://www.marlin.csiro.au/geonetwork/srv/eng/search#!c88d62e1-43a2-4790-9fe6-5e4be21023b9.

References:

Abel, S. J., D. N. Walters, and G. Allen, 2010: Evaluation of stratocumulus cloud prediction in the Met Office forecast model during VOCALW-REx. Atmos. Chem. Phys., 10, 10541-10559. Doi:10.5194/acp-10-10541-2010.

Alexander, S. P., & Protat, A. (2019): Vertical profiling of aerosols with a combined Raman-elastic backscatter lidar in the remote Southern Ocean marine boundary layer (43–66◦S,132–150◦E). Journal of Geophysical Research: Atmospheres, 124,12,107–12,125. https://doi.org/10.1029/2019JD030628

Alexander, S. P., and A. Protat, 2018: Southern Ocean cloud properties as observed from the surface and satellite. J. Geophys. Res. Atmos., 123. https://doi.org/10.1002/2017JD026552

Armour, K. C., J. Marshall, J. R. Scott, A. Donohoe, and E. R. Newsom, 2016: Southern Ocean warming delayed by circumpolar upwelling and equatorward transport, Nature Geoscience, doi: 10.1038/NGEO2731.

Ayers, G. P. and J. L. Gras, 1991: Seasonal relationship between cloud condensation nuclei and aerosol methanesulphonate in marine air. Nature, 353, 834-835.

Berry, E., G. G. Mace, and A. Gettelman, 2019: Using A-Train Observations to evaluate cloud occurrence and radiative effects in the Community Atmosphere Model during the Southeast Asia summer monsoon. J. Clim., 32, 4145-4165, DOI: 10.1175/JCLI-D-18-0693.1.

860 Berry, E., G. G. Mace, and A. Gettelman, 2020, Using A-Train observations to evaluate East
861 Pacific cloud occurrence and radiative effect in the Community Atmosphere Model.
862 Journal of Climate, Accepted, doi: 10.1175/JCLI-D-19-870.1

863 Bodas-Salcedo, A., K D. Williams, P. R. Field, and A. P. Lock, 2012: the surface downwelling solar
864 radiation surplus over the Southern Ocean in the Met Office Model: The role of
865 midlatitude cyclone clouds. Journal of Climate, 25, 7467-2498.

866 Bodas-Salcedo, A., K. D. Williams, M. A. Ringer, I. Beau, J. N. S. Cole, J. –L. Dufresne, T Koshiro, B.
867 Stevens, Z. Wang, and T Yokohata, 2014: Origins, of the solar radiation biases over the
868 Southern Ocean in CFMIP2 Models, Journal of Climate, 27, 41-57, DOI: 10.1175/JCLI-D-
869 13-00169.1

870 Bodas-Salcedo, A., P. Hill, K. Furtado, K. Williams, P. Field, J. Manners, P. Hyder, and S. Kato, 2016:
871 Large contribution of supercooled liquid clouds to the solar radiation budget of the
872 Southern Ocean. J. Climate. doi:10.1175/JCLI-D-15- 0564.1

873 Bodas-Salcedo, A., Mulcahy, J. P., Andrews, T., Williams, K. D., Ringer, M. A., Field, P. R., &
874 Elsaesser, G. S. (2019). Strong dependence of atmospheric feedbacks on mixed-phase
875 microphysics and aerosol-cloud interactions in HadGEM3. Journal of Advances in
876 Modeling Earth Systems, 11,1735–1758. https://doi.org/10.1029/2019MS001688

877 Damm, E., D. Nomura, A. Martin, G. S. Dieckmann, and K. M. Meiners, 2016: DMSP and DMS
878 cycling within Antarctic sea ice during the witner-spring transition. Deep-Sea Research II
879 131, 150-159, http://dx.doi.org/10.1016.j.dsr2.2015.12.015.

880 Deppeler SL and Davidson AT (2017) Southern Ocean Phytoplankton in a Changing Climate.
881 Front. Mar. Sci. 4:40.doi: 10.3389/fmars.2017.00040

882 Delanoë, J., et al. (2016), BASTA, a 95 GHz FMCW Doppler radar for cloud and fog studies, J.
883 Atmos. Oceanic Technol., 33, 1023–1038.

884 Fossum, K. N., J. Ovadnevaite, D. Ceburnis, M. Dall'Osto, S. Marullo, M. Bellaicco, R. Simo, D Liu,
885 M Flynn, A. Zuend, and C. O'Dowd, 2018: Summertime primary and secondary
886 contributions to Southern Ocean Cloud Condensation Nuclei, Scientific Reports, 8:
887 13844, doi:10.1038/s41598-018-32047-4.

888 Frey, W. R. and J. E. Kay, 2017: The influence of extratropical cloud phase and amount
889 feedbacks on climate sensitivity. Clim. Dyn. DOI: 10.1007/s00382-017-3796-5.

890 Fröhlich, R., Cubison, M. J., Slowik, J. G., Bukowiecki, N., Prévôt, A. S. H., Baltensperger, U.,
891 Schneider, J., Kimmel, J. R., Gonin, M., Rohner, U., Worsnop, D. R., and Jayne, J. T.: The
892 ToF-ACSM: a portable aerosol chemical speciation monitor with TOFMS detection,
893 Atmos. Meas. Tech., 6, 3225–3241, https://doi.org/10.5194/amt-6-3225-2013, 2013.

Gettelmen, A., C. G. Bardeen, C. S. McCluskey, E. Jarvinen, J. Stith, and C. Bretherton, 2020: Simulating observations of Southern Ocean clouds and implications for climate. Submitted to Journal of Geophysical Research.

Gordon, N. D., and S. A. Klein (2014), Low-cloud optical depth feedback in climate models, J. Geophys. Res. Atmos., 119, 6052–6065, doi:10.1002/2013JD021052.

Giles, E. and Klepinger, L., "Confidence Intervals for Estimates Based on Linear Regression in Forensic Anthropology," *Journal of Forensic Sciences*, Vol. 33, No. 5, 0, pp. 1218-1222, https://doi.org/10.1520/JFS12555J. ISSN 0022-1198

Hu, Y., et al., 2009: CALIPSO/CALIOP cloud phase discrimination algorithm, Journal of Atmospheric and Oceanic Technology, 26, 2293-2309, DOI: 10.1175/2009JTECHA1280.1

Hu, Y., S. Rodier, K-m. Xu, W. Sun, J. Huang, B. Lin, P. Zhai, and D. Josset, 2010: Occurrence, liquid water content, and fraction of supercooled water clouds from combined SALIOP/IIR/MODIS measurements. 2010: JOURNAL OF GEOPHYSICAL RESEARCH, VOL. 115, D00H34, doi:10.1029/2009JD012384, 2010

Huang, Y., S. T. Siems, M. J. Manton, D. Rosenfeld, R. Marchand, G. M. McFarquhar, and A. Protat, 2016: What is the role of sea surface temperature in modulating cloud and precipiation properties over the Southern Ocean? Journal of Climate, 29, 7453-7473, doi: 10.1175/JCLI-D-15-0768.1

Humphries, R. S., A. R. Klekociuk, R. Schofield, M. Keywood, J. Ward, and S. R. Wilson, 2016: Unexpectedly high ultrafine aerosol concentration above East Antarctic sea ice. Atmos. Chem. Phys. 16, 2185-2206, doi:10.5192/acp-16-2185-2016.

Kay, J. E., Wall, C., Yettella, V., Medeiros, B. Hannay, C., P. Caldwell, and C. Bitz, 2016: Global climate impacts of fixing the Southern Ocean shortwave radiation bias in the Community Earth System Model, J. Climate, doi:10.1175/JCLI-D-15-0358.1

Kelleher, M. K., and K. M. Grise, 2019: Examining Southern Ocean Cloud Controlling Factors on Daily time scales and their connections to midlatitude weather systems. Journal of Climate, 32, 5145-5159, doi: 10.1175/JCLI-D-18-0840.1

Klein, S. A., A. Hall, J. R. Norris and R. Pincus, 2017: Low-cloud feedbacks from cloud-controlling factors: A review. Surv. Geophys., 38, 1307-1329, https://doi.org/10.1007/s10712-017-9433.3.

Kato, S., G. L. Smith, and H. W. Barker, 2001: Gamma-weighted discrete ordinate two-stream approximation for computation of domain-averaged solar irradiance. J. Atmos. Sci., 58, 3797-3803.

927 Kennicutt II, M. C., and Co-Authors, 2014: A roadmap for Antarctic and Southern Ocean science
928 for the next two decades and beyond, 2014: Antarctic Science, 27(1), 3-18.

929 Kirk, P. D. W., M. P. H. Stumpf, 2009: Gaussian process regression bootstrapping: Exploring the
930 effects of uncertainty in time course data. Bioinformatics, 25, `1300-1306.

931 Klepp, C., S. Michel, A. Protat, J. Burdanowitz, N. Albern, A. Dahl, M. Kähnert, V. Louf, S. Bakan,
932 and S. A. Buehler, 2018: OceanRAIN, a new in-situ shipboard global ocean surface-
933 reference dataset of all water cycle components. Nature – Scientific Data, DOI:
934 10.1038/sdata.2018.122.

935 Kollias, P., B. P. Treserras, and A., Protat, 2019: Calibration of the 2007-2017 record of ARM
936 cloud radar observations using CloudSat. Atmos. Meas. Tech. 12, 4949-4964,
937 https://doi.org/10.5194/amt-12-4949-2019.

938 Krüger, O., and H. Graßl, 2011: Southern Ocean phytoplankton increases cloud albedo and
939 reduces precipitation, Geophysical Research Letters, 38, L08809, DOI:
940 10.1029/2011GL047116.

941 Li, J. Y. Hu., J. Huang, K. Stamnes, Y. Yi, and S. Stamnes, 2011: A new method for retrieval of the
942 extinction coefficient of water clouds by using the tail of the CALIOP signal. Atmos.
943 Chem. Phys., 11, 2903-2916, doi: 10.5194/acp-11-2903-2011.

944 Liljegren, J. C.,1994: Two-channel microwave radiometer for observations of total column
945 precipitable water vapor and cloud liquid water path, paper presented at the Fifth
946 Symposium on Global Change Studies, Am. Meteorol. Coc., Nashville, Tenn. Jan. 23-28.

947 Liljegren, J. C., E. E. Clothiaux, G. G. Mace, S. Kato, X. Dong, 2001: A new retrieval for cloud
948 liquid water path using a ground-based microwave radiometer and measurements of
949 cloud temperature. Journal of Geophysical Research, Vol. 106, No. D13, 14,485-14,500.

950 Liu, W. J. Lu, S.-P. Xie, and Alexey Fedorov, 2018: Southern Ocean heat uptake , redistribution
951 and storage in a warming climate: The role of meridional overturning circulation. Journal
952 of Climate, 31, 4727-4743, DOI: 10.1175/JCLI-D-17-07061.1.

953 Lu, M.-L. and A. Sorooshian, H. H. Jonsson, G. Feingold, R. C. Flagan, J. H. Seinfeld, Marine
954 stratocumulus aerosol-cloud relationships in the MASE II experiment: Precipitation
955 susceptibility in Eastern Pacific marine stratocumulus, Journal of Geophysical Research,
956 114, doi:10.1029/2009JD012774.

957 Mace, G. G., Sally Benson, and Y. Hu, 2020: On the frequency of the occurrence of the ice phase
958 in supercooled Southern Ocean low clouds derived from CALIPSOI and CloudSat.
959 Geophysical Research Letters, In press, https://doi.org/10.1029/2020GL087554.

960 Mace, G. G., and S. Avey, 2017: Seasonal variability of warm boundary layer clouds and
961 precipitation properties in the Southern Ocean as diagnosed from A-Train data. Journal
962 of Geophysical Res. Atmos., 122, 1015-1032, doi:10.1002/2016JD025348.

963 Mace, G. G., Q Zhang, M. Vaughn, R. Marchand, G. Stephens, C. Trepte, D. Winker, 2009: A
964 description of hydrometeor layer occurrence statistics derived from the first year of
965 merged Cloudsat and CALIPSO data. J. Geophys. Res., 114,D00A26,
966 doi:10.1029/2007JD009755.

967 Mace G. G., 2010: Cloud properties and radiative forcing over the maritime storm tracks of the
968 Southern Ocean and North Atlantic derived from A-Train. Journal of Geophysical
969 Research, 115, doi:10.1029/2009JD012517.

970 Mace, G. G. and Zhang, 2014: The Cloudsat Radar-Lidar Geometrical Profile Algorithm (RL-
971 GeoProf): Updates, Improvements, and Selected Results. Journal of Geophysical
972 Research, DOI: 10.1002/2013JD021374.

973 Mace G. G., and B. Berry, 2017: Using active remote sensors to evaluate cloud-climate
974 feedbacks: A review and and look to the future. Current Climate Change Reports, DOI
975 10.1007/s40641-017-0067-9.

976 Mace, G. G., S. Avey, S. Cooper, M. Lebsock, S. Tanelli, and G. Dobrowalski, 2016: Retrieving co-
977 occurring cloud and precipitation properties of warm marine boundary layer clouds with
978 A-Train data. J. Geophys. Res. 120, doi:10.1002:/2015JDO23681.

979 Marchand, R., G. G. Mace, T. Ackerman, and G. Stephens, 2008: Hydrometeor detection using
980 CloudSat – an Earth-orbiting 94-GHz cloud radar. Journal of Atmospheric and Oceanic
981 Technology. 25, doi:10.1175/2007JTECHA1006.1, 519-533.

982 Maahn, Masimillian, D. D. Turner, U. Lohnert, D. J. Posselt, Kerstin Ebell, G. G. Mace, and J. M.
983 Comstock. 2020: Optimal estimation retrievals and their uncertainties: What every
984 atmospheric scientist should know. Bull. Amer. Meteor. Soc.
985 https://doi.org/10.1175/BAMS-D-19-0027.1.

986 McCoy D. T., S. M. Burrows, R. Wood, D. P. Grosvenor, S. M. Elliott, P. Ma, P. J. Rasch, and D.
987 Hartmann, 2015: Natural aerosols explain seasonal and spatial patterns of Southern
988 Ocean cloud albedo. Sci. Adv. 1, e1500157.

989 McCoy D. T., P. R. Field, G. S. Elsaesser, A. Bodas-Salcedo, B. H. Kahn, M, D. Zelinka, C. Kodama,
990 T. Mauritsen B. Vanniere, M. Roberts, P. L. Vidale, D. Saint-Martin, A. Voldoire, R.
991 Haarsma, A. Hill, B. Shipway, and J. Wilkonson, 2019: Cloud feedbacks in extratropical
992 cyclones: Insights from long-term satellite data and high resolution global simulations.
993 Atmos. Chem. Phys., 19, 1147-1172, https://doi.org/10.5194/acp-19-1147-2019.

McFarquhar, G. and 42 coauthors, 2020: Unique observations of clouds, aerosols, precipitation, and surface radiation over the Southern Ocean: An overview of CAPRICORN, MARCUS, MICRE, and SOCRATES. Submitted to the Bulletin of the American Meteorological Society.

O'Connor, E. J., et al., (2004): A technique for autocalibration of cloud lidar, J. Atmos. Oceanic. Technol., 21, 777-786.

Painemal, D. and P. Zuidema, 2013: The first aerosol indirect effect quantified through airborne remote sensing during VOCALS-Rex. Atmos. Chem. Phys. 13, 917-931, doi:10.5194/acp-13-917-2013.

Painemal, D. and P. Minnins, 2012: On the dependence of albedo on cloud microphysics over marine stratocumulus clouds regimes determined from Clouds and the Earth's Radiant Energy System (CERES) data. Journal of Geophysical Research, 117, D06203, doi:10.1029/2011JD017120.

Platnick, S., and S. Twomey, 1994: Determining the susceptibility of cloud albedo to changes in droplet concentration with Advanced Very High Resolution Radiometer. Journal of Applied Meteorology, 33, 334-347.

Platt, C. M. R., D. M. Winker, M. A. Vaughan, and S. D. Miller, 1999: Backscatter-to-extinction ratios in the top layers of tropical mesoscale convective systems and in isolated cirrus from LITE obsevations. Journal of Applied Meteorology, 38, 1330-1345.

Protat, A., E. Schulz, L. Rikus, Z. Sun, and Y. Xiao, 2017: Shipborne observations of the radiative effect of Southern Ocean Clouds. J. Geophys. Res. Atmos., 122, 318-328.

Protat, A., D. Bouniol, E. J. O'Connor, H. K. Baltink, J. Verlinde, and K. Widener, 2011: CloudSat as a Global Radar Calibrator. J. Atmos. Oceanic Tech., 28, 445-452.

Rauber, R. M. and co-authors, 2006: Rain in shallow cumulus over the ocean; the RICO campaign. Bulletin of the American Meteorological Society, 87, 1912-1919.

Royer, P., A. Bizard, L. Sauvage, and L. Thobois, 2014: Validation protocol and intercomparison campaigns with the R-MAN510 aerosol lidar. Proc. 17th Int. Symp. for the Advancement of Boundary-Layer Remote Sensing, Auckland, New Zealand, ISARS, XX–XX.

Savic-Jovcic, V. and B. Stevens, 2008: The structure and mesoscale organization of precipitating stratocumulus. J. Atmos. Sciences, 65, 1587-1605.

Schulz, E. W., S. A Josey, and R. Verein, 2012: First air-sea flux mooring meaurements in the Southern Ocean, Geophysical Research Letters, 39, doi. 10.1029/2012GL052290.

Shaw G. E. 1988: Antarctic Aerosols: A Review. Reviews of Geophysics, 26, 1, 89-112.

1026 Stephens, G. L., et al. (2008), CloudSat mission: Performance and early science after the first year
1027 of operation, J. Geophys. Res., 113, D00A18, doi:10.1029/2008JD009982.

1028 Tan, I., T. Storelvmo, and M. D. Zelinka, 2016: Observational constraints on mixed phase clouse
1029 imply higher climate sensitivity. Science, 352, 224-228, doi: 10.1126/science.aad5300.

1030 Tanelli, S., S. L. Durden, E. Im, K. S. Pak, D. G. Reinke, P. Partain, J. M Haynes, and R. T.
1031 Marchand, 2008: CloudSat's Cloud Profiling Radar after two years in orbit: Performance,
1032 calibration, and processing. IEEE Transaction on Geoscience and Remote Sensing, 46,
1033 3650-3663, DOI: 10.1109/TGRS.2008.2002030.

1034 Terai, C. R., Zhang, Y., Klein, S. A., Zelinka, M. D., Chiu, J. C., & Min, Q. (2019). Mechanisms
1035 behind the extratropical stratiform low-cloud optical depth response to temperature in
1036 ARM site observations. Journal of Geophysical Research: Atmospheres, 124, 2127–2147.
1037 https://doi.org/10.1029/2018JD029359

1038 Toon, O. B., C. P. McCay, T. P. Ackerman, and K. Santhanam, 1989: Rapid calculation of radiative
1039 heating rate and photodissociation rates in inhomogeneous multiple scattering
1040 atmospheres. J. Geophys. Res., 94, 16,287-16,301.

1041 Trenberth, Kevin E., John T. Fasullo, 2010: Simulation of Present-Day and Twenty-First-Century
1042 Energy Budgets of the Southern Oceans. J. Climate, 23, 440–454. DOI
1043 10.1175/2009JCLI3152.1

1044 Twomey, S. 1977: The influence of pollution o the shortwave albedo of clouds. Journal of the
1045 Atmospheric Sciences, 34, 1149-1152.

1046 Vergara-Temprado, J., A. K. Miltenberger, K. Furtado, D. P. Grosveno, B. J. Shipway, A. A. Hill, J.
1047 M. Wilkinson, P. R. Field, B. J. Murray, and K. S. Carslaw, 2018: Strong control of
1048 Southern Ocean cloud reflectivity by ice nucleating particles. Proceedings of the
1049 National Academy of Sciences, doi: 10.1073/pnas.1721627115.

1050 Wang, Y., G. M. McFarquhar, R. M. Rauber, C. Zhao, W. Wu, J. A. Finlon, D. M. Stechman, J.
1051 Stith, J. B. Jensen, M. Schnaiter, E. Jarvinen, F. Waitz, J. Vivekeanandan, M. Dixon, B.
1052 Rainwater, and D. W. Twohy, 2020: Microphysical properties of generating cells over the
1053 Southern Ocean: Results from SOCRATES. Accepted Journal of Geophysical Research.

1054 Winker, D. M., M. A. Vaughan, A. Omar, Y. Hu, K. Powell, Z. Liu, W. H. Hunt, S. A. Young, 2009:
1055 Overview of the CALIPSO mission and CALIOP data processing algorithms. Journal of
1056 Atmospheric and Oceanic Technology, 26, 2310-2324, DOI: 10.1175/2009JtechA1281.1

1057 Zuidema, P., Xue, H., & Feingold, G. (2008). Shortwave radiative impacts from aerosol effects on
1058 marine shallow cumuli. *Journal of the Atmospheric Sciences*, *65*(6), 1979-
1059 1990. https://doi.org/10.1175/2007JAS2447.1

Table Captions:

Table 1: Table 1: Vertical occurrence data from CloudSat (Stephens et al., 2008) and CALIPSO (Winker et al., 2009) between 2007-2010 using the combined characterization of Mace and Zhang, (2014) in the 40s-70s latitude belt.

Figure Captions:

Figure 1. Voyage tracks taken R/V Investigator and Aurora Australis during CAPRICORN I and II and MARCUS

Figure 2. January 29 Case Study collected during CAPRICORN II. a) radar reflectivity from the BASTA W-Band Radar. Lidar derived cloud base is marked by white dots. b) Lidar attenuated backscatter, c) lidar layer-integrated depolarization ratio (red) and multiple scattering factor (black), d) difference of 31 GHz Tb from cloud-free sky (black) and lidar depolarization ratio at cloud base. e) Retrieved Liquid water path with uncertainty marked by the error bars. f) retrieved effective radius with error bars. g) retrieved cloud droplet number with error bars. h) Aerosol Sulfate mass and CCN at 0.5% supersaturation.

Figure 3. Comparison of sub cloud radar reflectivity from liquid hydrometeors observed by the calibrated BASTA W-Band radar and the MARCUS MWACR during the months of January and February (red).

Figure 4. Cloud and radiation property frequency distributions compiled from the retrieved microphysical properties using data from MARCUS and CAPRICORN I and II. Red histograms show observations compiled from in situ airborne data from SOCRATES (b and c) and from the ship pyranometer (h). a) Liquid water path, b) Effective radius with red showing the effective radius frequency from the SOCRATES in situ data c) Cloud Droplet Number Concentration with red as in b. d) uncertainty distribution of LWP, e) uncertainty distribution of effective radius, f) uncertainty distribution of cloud droplet number. g) Distribution of the difference of calculated downwelling solar flux from that observed at the ship. h) Calculated fraction of the downwelling solar flux at the surface removed from the clear sky flux by the clouds. I) scatterplot of albedo calculated from the cloud properties as a function of visible optical depth.

Figure 5. Derived cloud and radiation properties. a) Albedo Susceptibility. Red shows southern analysis domain. Black shows middle and northern domains combined. Error bars show 95% confidence interval of the linear regression slope. b) liquid water path as a function cloud droplet number concentration color coded by effective radius with black: sub 5 um, blue: 5-7 um, red: 7-9 um, orange: 9-11 um), yellow: > 11 um. The black cure with symbols show the mean LWP in cloud droplet number bins. b) Albedo Susceptibility (dA/dln(Nd)). Red is the

1095 southern analysis domain. Black is the northern and middle domains. c) Albedo as function of
1096 optical depth with color coded re as in a. d) Albedo as a function of Nd color coded for LWP
1097 with black less than 50 g m-2, blue denotes LWP from 50-100 g m-2, and orange denotes LWP
1098 from 100 to 150 g m-2. The lines denote linear regressions of albedo as a function of Nd in the
1099 LWP bins representing the albedo susceptibility as depicted in a.

1100 Figure 6. Latitudinal variations of retrieved cloud and derived radiative properties. solid black
1101 denotes the northern analysis domain. Dashed denotes the middle latitude domain. Red
1102 denotes the Southern Latitude domain. See text for details

1103 Figure 7. As in Figure 4 except for the 2-5 January 2018 Marcus Case Study when the Aurora
1104 Australis was docked at Casey Station Antarctica.

1105 Figure 8. Regression of visible optical depth of the liquid phase non precipitating clouds as a
1106 function of layer temperature for the combined Capricorn and Marcus data sets.
1107

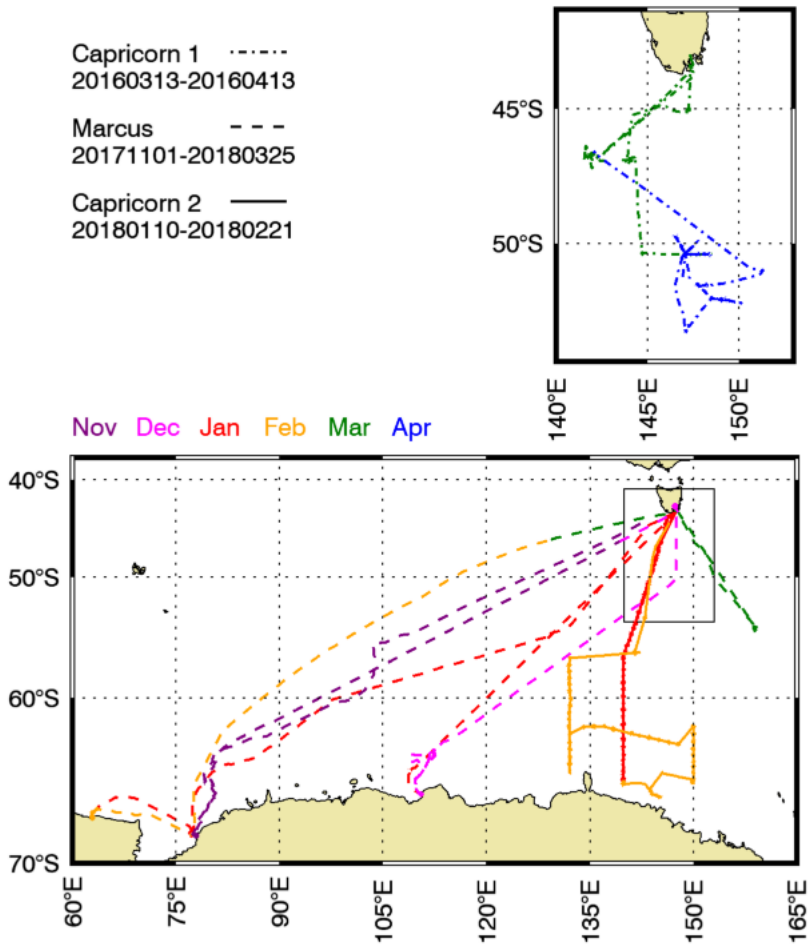

Figure 1. Voyage tracks taken R/V Investigator and Aurora Australis during CAPRICORN I and II and MARCUS

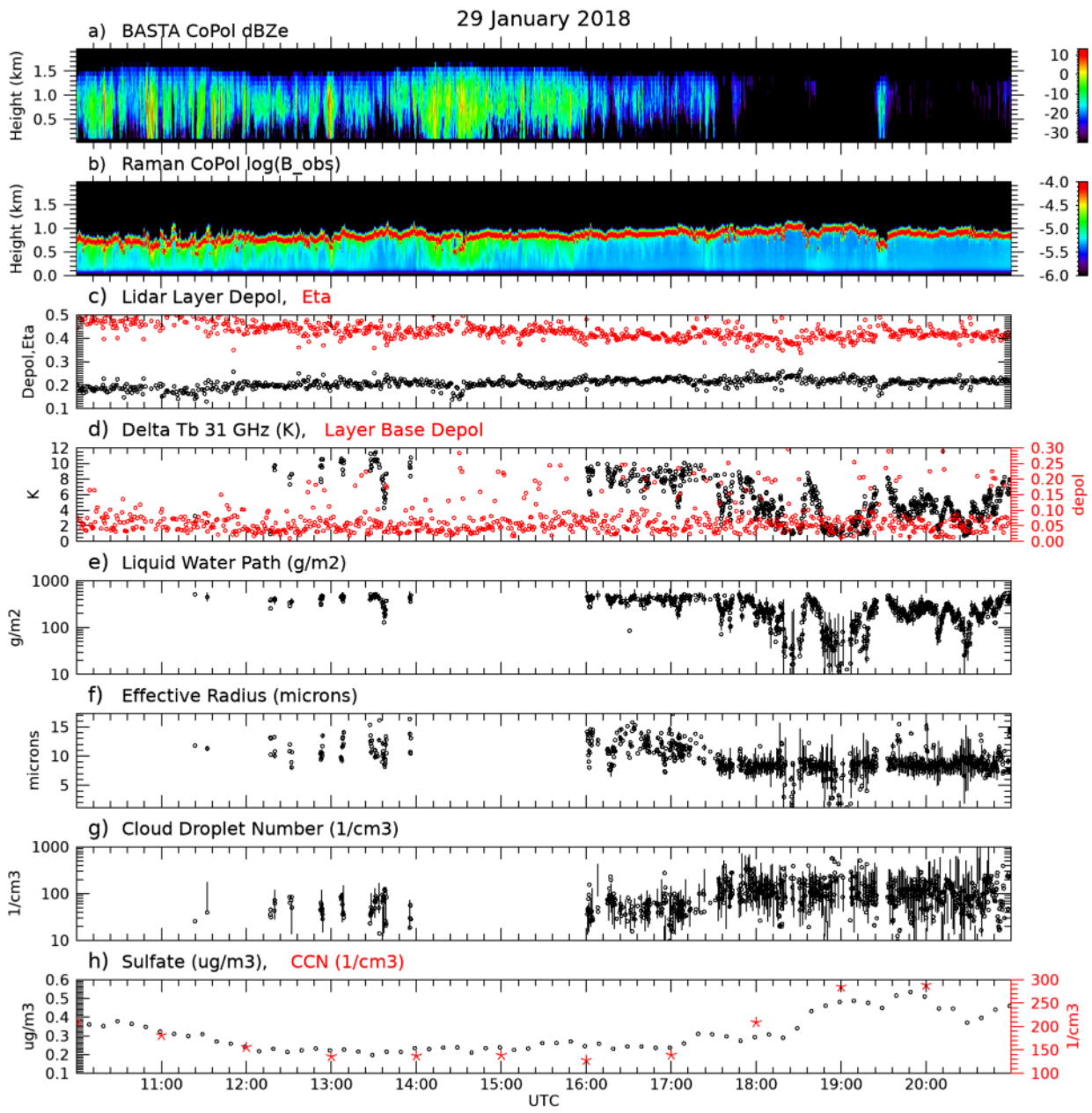

Figure 2. January 29 Case Study collected during CAPRICORN II. a) radar reflectivity from the BASTA W-Band Radar. Lidar derived cloud base is marked by white dots. b) Lidar attenuated backscatter, c) lidar layer-integrated depolarization ratio (red) and multiple scattering factor (black), d) difference of 31 GHz Tb from cloud-free sky (black) and lidar depolarization ratio at cloud base. e) Retrieved Liquid water path with uncertainty marked by the error bars. f) retrieved effective radius with error bars. g) retrieved cloud droplet number with error bars. h) Aerosol Sulfate mass and CCN at 0.5% supersaturation.

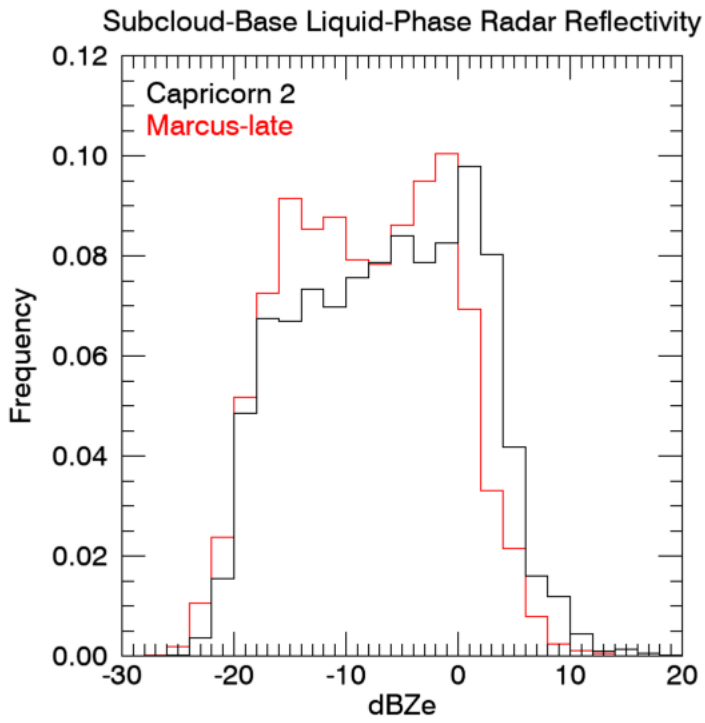

Figure 3. Comparison of sub cloud radar reflectivity from liquid hydrometeors observed by the calibrated BASTA W-Band radar and the MARCUS MWACR during the months of January and February (red).

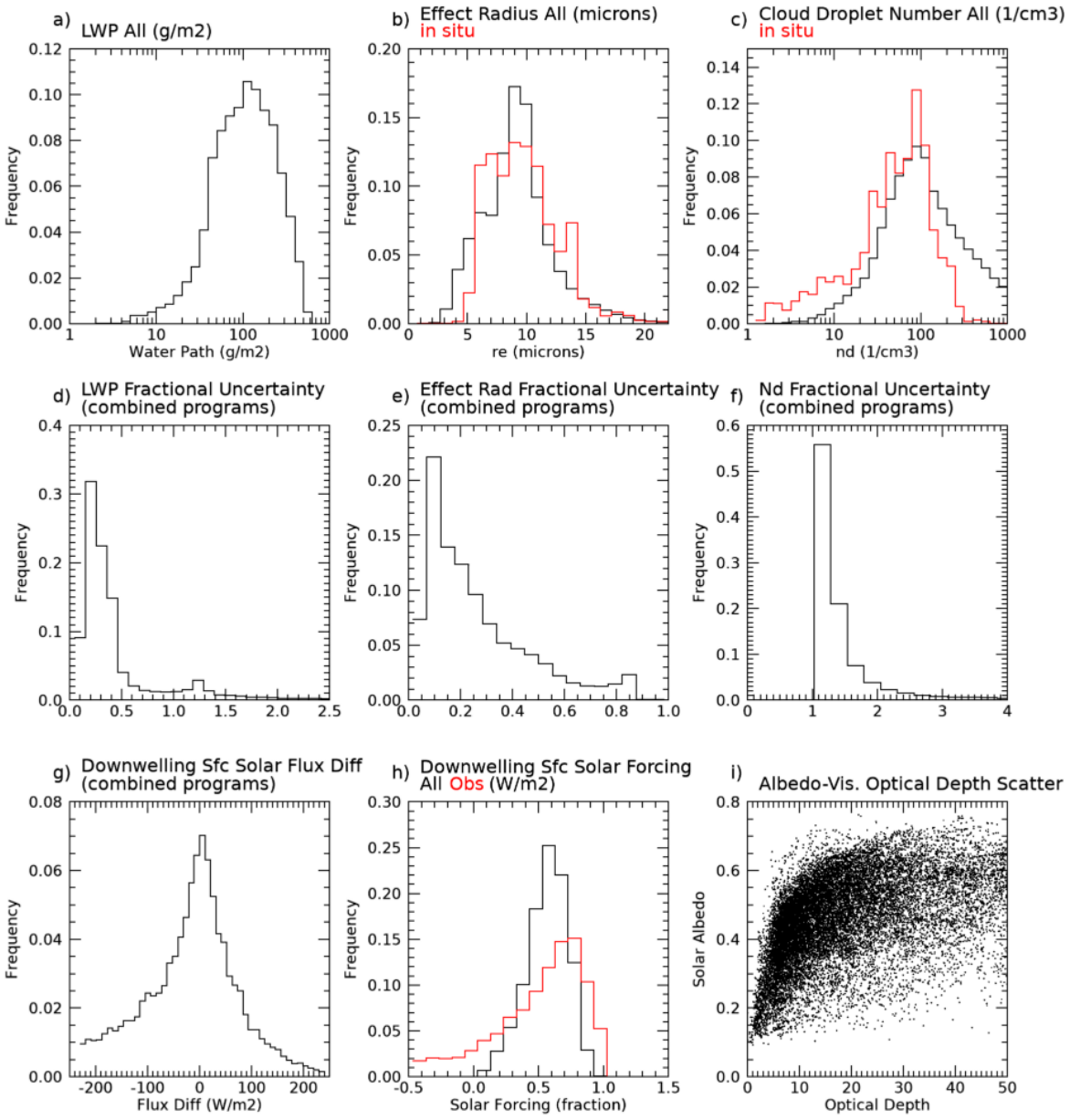

Figure 4. Cloud and radiation property frequency distributions compiled from the retrieved microphysical properties using data from MARCUS and CAPRICORN I and II. Red histograms show observations compiled from in situ airborne data from SOCRATES (b and c) and from the ship pyranometer (h). a) Liquid water path, b) Effective radius with red showing the effective radius frequency from the SOCRATES in situ data c) Cloud Droplet Number Concentration with red as in b. d) uncertainty distribution of LWP, e) uncertainty distribution of effective radius, f) uncertainty distribution of cloud droplet number. g) Distribution of the difference of calculated downwelling solar flux from that observed at the ship. h) Calculated fraction of the downwelling solar flux at the surface removed from the clear sky flux by the clouds. I) scatterplot of albedo calculated from the cloud properties as a function of visible optical depth.

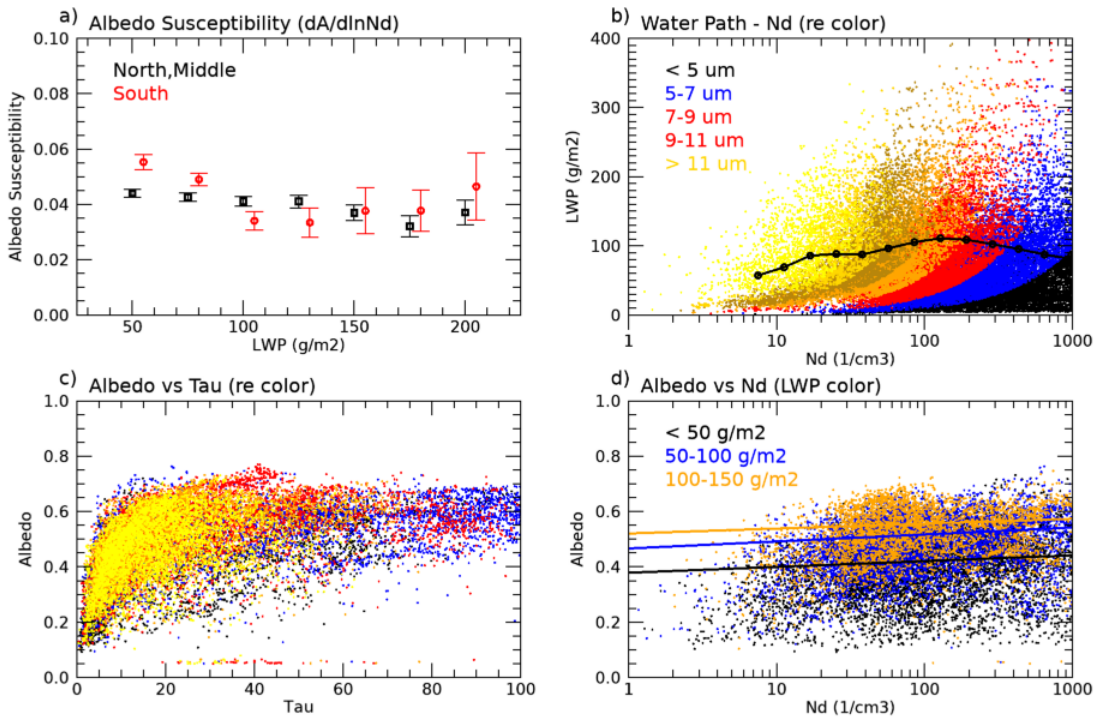

Figure 5. Derived cloud and radiation properties. a) Albedo Susceptibility. Red shows southern analysis domain. Black shows middle and northern domains combined. Error bars show 95% confidence interval of the linear regression slope. b) liquid water path as a function cloud droplet number concentration color coded by effective radius with black: sub 5 um, blue: 5-7 um, red: 7-9 um, orange: 9-11 um), yellow: > 11 um. The black cure with symbols show the mean LWP in cloud droplet number bins. b) Albedo Susceptibility (dA/dln(Nd)). Red is the southern analysis domain. Black is the northern and middle domains. c) Albedo as function of optical depth with color coded re as in a. d) Albedo as a function of Nd color coded for LWP with black less than 50 g m-2, blue denotes LWP from 50-100 g m-2, and orange denotes LWP from 100 to 150 g m-2. The lines denote linear regressions of albedo as a function of Nd in the LWP bins representing the albedo susceptibility as depicted in a.

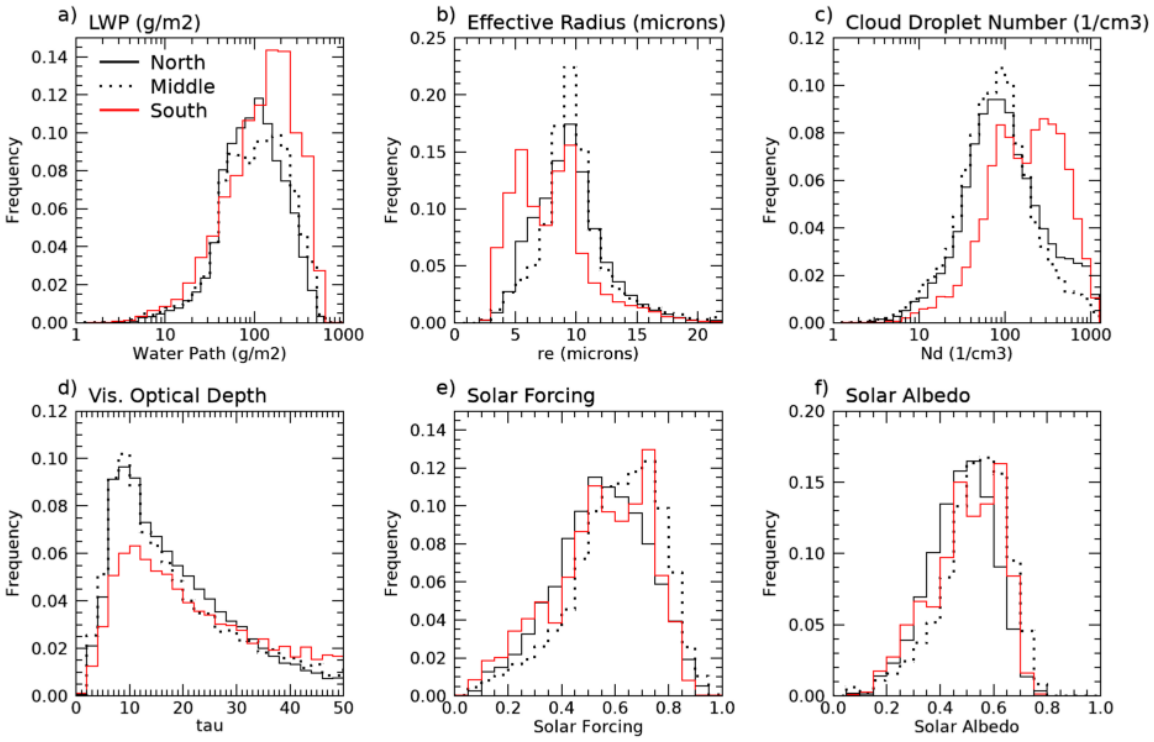

Figure 6. Latitudinal variations of retrieved cloud and derived radiative properties. solid black denotes the northern analysis domain. Dashed denotes the middle latitude domain. Red denotes the Southern Latitude domain. See text for details

1159
1160
1161

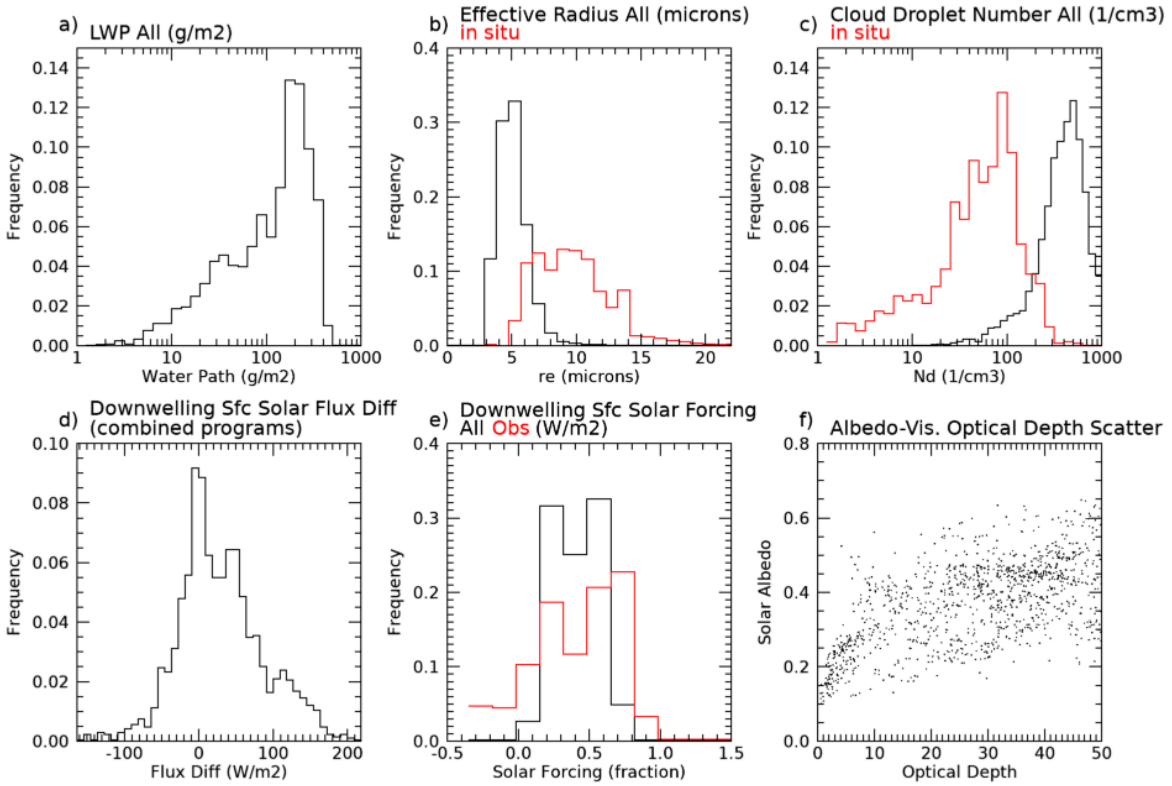

Figure 7. As in Figure 4 except for the 2-5 January 2018 Marcus Case Study when the Aurora Australis was docked at Casey Station Antarctica.

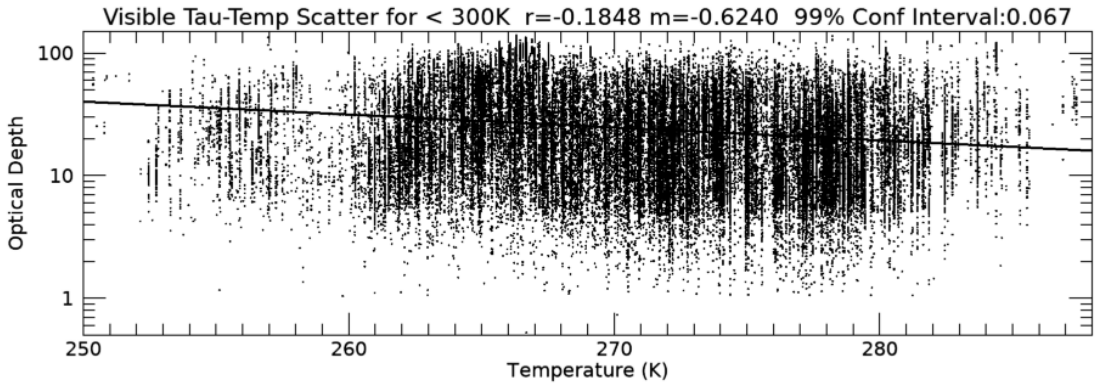

Figure 8. Regression of visible optical depth of the liquid phase non precipitating clouds as a function of layer temperature for the combined Capricorn and Marcus data sets.